

# Thesis

Ekaterina Avdeeva

University of Nebraska-Lincoln, USA

December 7, 2016

## Abstract

This paper reviews

## Contents

|    |          |   |           |
|----|----------|---|-----------|
| 8  | <b>1</b> | <b>Introduction</b>   | <b>2</b>  |
| 9  | 1.1      | Fundamental Particles and Interactions . . . . .                              | 3         |
| 10 | 1.2      | Electroweak Interactions . . . . .  | 5         |
| 11 | 1.3      | Strong Interactions . . . . .   | 8         |
| 12 | 1.4      | Physics of Proton-Proton Collisions . . . . .                                 | 9         |
| 13 | 1.5      | Open Questions of the Standard Model . . . . .                                | 11        |
| 14 | <b>2</b> | <b><math>W\gamma</math> Production Theory and Former Experimental Results</b> | <b>12</b> |
| 15 | 2.1      | Electroweak Theory of the Standard Model . . . . .                            | 13        |
| 16 | 2.2      | Cross Section and Luminosity . . . . .  | 18        |
| 17 | 2.3      | Standard Model $W\gamma$ Production . . . . .                                 | 20        |
| 18 | 2.4      | Anomalous $W\gamma$ Production . . . . .                                      | 22        |
| 19 | 2.5      | Measurements in the Past . . . . .  | 25        |
| 20 | <b>3</b> | <b>Experimental Setup</b>   | <b>27</b> |
| 21 | 3.1      | Large Hadron Collider . . . . .   | 28        |
| 22 | 3.2      | Compact Muon Solenoid . . . . .   | 31        |
| 23 | 3.2.1    | Introduction . . . . .  | 31        |
| 24 | 3.2.2    | Magnet . . . . .  | 32        |
| 25 | 3.2.3    | Tracking System . . . . .   | 32        |
| 26 | 3.2.4    | Electromagnetic Calorimeter . . . . .   | 33        |
| 27 | 3.2.5    | Hadron Calorimeter . . . . .  | 34        |
| 28 | 3.2.6    | Muon System . . . . .   | 34        |
| 29 | 3.2.7    | Triggering and Data Aquisition . . . . .                                      | 35        |
| 30 | 3.2.8    | Event Reconstruction . . . . .  | 35        |
| 31 | <b>4</b> | <b>CMS Tracker Alignment</b>  | <b>38</b> |
| 32 | 4.1      | Algorithm . . . . .   | 39        |
| 33 | 4.2      | Selected Results . . . . .  | 44        |
| 34 | <b>5</b> | <b><math>W\gamma</math> Cross Section Measurement</b>                         | <b>45</b> |

## 35 1 Introduction

36 Elementary particle physics describes our world in terms of its smallest constituents, fundamen-  
37 tal particles, and their interactions. Going from larger to smaller scales, substances around us  
38 consist of molecules, molecules consist of atoms, in an atom, there is a nucleus made of neutrons  
39 and protons and some number of electrons occupying their orbits around the nucleus. Protons  
40 and neutrons have a structure while an electron is not known to have any structure, therefore,  
41 an electron is an example of a particle which is considered to be fundamental.

42 Interactions of elementary particles are described by quantum field theories which incorporate  
43 principles of the quantum mechanics and the special theory of relativity. The set of such theories,  
44 including quantum elecrtrodynamics (QED), quantum chromodynamics (QCD) and the theory  
45 of weak interactions is called the Standard Model (SM). It has been proven to be an accurate  
46 description of interactions of elementary particles observed by now.

47 However, there are several experimental observations which are not described by the SM such  
48 as gravity, dark matter, dark energy, matter/antimatter asymmetry and others. Therefore, the  
49 SM is not the complete theory of particle interactions. There are several SM extensions offered by  
50 theorists as well as radically new theories waiting for the experimental confirmation or disproof.

51 Some SM extensions and new theories predict the existence of heavy particles mass of which  
52 possibly lies beyond experimentally reachable energies. The search of these particles is one of the  
53 prioritized directions in particle physics. One source of highly energetic elementary particles is  
54 cosmic rays. The most energetic particles ever observed came from this source. However, cosmic  
55 rays are totally uncontrollable and such highly energetic particles are rare. If we want to produce  
56 a large number of particles in a given energy range, we need to use a particle accelerator. A  
57 large amount of data allows experimentalists to perform a statistical analysis and increase the  
58 probability to find a new particle if it exists.

59 Symmetric colliding beams is the most effective way to produce as heavy particles as possible  
60 given the energies of the colliding particles. Comparing to experiments of colliding a single beam  
61 to a fixed target, in case of a symmetric collision the total momentum of two colliding particles  
62 is zero and, therefore, much larger fraction of energy can transfer to a mass of a new particle.  
63 The Large Hadron Collider (LHC) is such a collider with the highest energy in the world ever  
64 built. It can produce the most massive particles to probe physics beyond the SM. It collides two  
65 proton ( $p p$ ) beams, two lead ion beams ( $Pb - Pb$ ) or a proton beam to a lead ion beam ( $p - Pb$ ).  
66 The design energies for a colliding proton and a colliding lead ion at LHC are 7 TeV and 522 TeV  
67 respectively.

68 Compact Muon Solenoid (CMS) is one of two general-purpose detectors at the LHC. It is  
69 placed at one of six collision points. CMS has a wide physics program including searches for the  
70 beyond SM (BSM) physics as well as the precision measurements of the SM parameters them-  
71 selves.

72 The total and the differential cross section with respect to the photon transverse momentum  
73 ( $P_T^\gamma$ ) has been measured. The  $P_T^\gamma$  is sensitive to the potential anomalous TGC (aTGC) in the  
74 high  $P_T^\gamma$  region. The disagreement between the measured and theoretically predicted differential  
75 cross section at the higher  $P_T^\gamma$  end would be an indication of the possible presence of the aTGC.

76 The rest of this chapter gives general introductory information about the SM while chapter  
77 2 concentrates on the theory of the SM and BSM  $W\gamma$  production and also discusses previous  
78 measurements of this process. Chapter 3 describes LHC and CMS in more details. Chapter  
79 4 explaines on specific aspect of the CMS operation which is the tracker alignment. Finally,  
80 chapter 5 describes the details of the measurement of this dissertation and reports the results.

## 89 1.1 Fundamental Particles and Interactions

90 The SM describes interactions of elementary particles. There are four fundamental interactions:  
91 electromagnetic, strong, weak and gravitational. The gravity is not included into the SM but its  
92 effect on particles is negligible compared to the other forces which makes it possible to develop a  
93 theory of the particle physics and conduct experiments even without having the gravity included  
94 into the model.

95

96 All fundamental elementary particles in the SM can be split into three categories by their  
97 spins. There are fermions which possess spin  $s=1/2$ , there are gauge bosons which are vector  
98 particles ( $s=1$ ) and there is the Higgs boson which is a scalar particle ( $s=0$ ).

99

100 The fermions are arranged into three generations, each generation consists of a quark with  
101 charge  $Q=+2/3$  (up, charm, and top quarks), a quark with  $Q=-1/3$  (down, strange, and bottom  
102 quarks), a charged lepton with  $Q=-1$  (electron, muon, and tau-lepton) and a neutrino (electron,  
103 muon, and tau neutrinos) which is electrically neutral. Each quark can carry any of three colors:  
104 red, blue, or green. Additionally, each fermion has its antiparticle. Therefore, the total number  
105 of fundamental fermions is  $(6(\text{leptons}) + 6(\text{quarks}) \cdot 3(\text{colors})) \cdot 2(\text{to include antiparticles}) = 48$ .

106

107 Corresponding particles in different generations have the same charges, spins and interaction  
108 properties but masses of particles increase with a generation. These mass differences lead to  
109 different decay properties because a particle A can decay to particles B and C only if the mass of  
110 A  $m_A > m_B + m_C$ . Thus, an electron is a stable particle, a muon decays as  $\mu^- \rightarrow e^- + \bar{\nu}_e + \nu_\mu$ ,  
111 a tau-lepton, as the heaviest charged lepton, has the largest number of decay channels amongst  
112 the charged leptons:  $\tau^- \rightarrow \mu^- + \bar{\nu}_\mu + \nu_\tau$ ,  $\tau^- \rightarrow e^- + \bar{\nu}_e + \nu_\tau$ ,  $\tau^- \rightarrow \nu_\tau + \text{quarks}$ .

113

114 In addition to fermions, the SM includes gauge bosons which are interaction mediators. They  
115 are called mediators because fermions interact with each other by exchanging them. For example,  
116 two charged fermions can interact with each other by exchanging a photon. Such interaction  
117 is called electromagnetic interaction and a photon is a mediator for the electromagnetic inter-  
118 action. Similarly, a gluon is a mediator for the strong interactions, and  $W^\pm$  and  $Z^0$  bosons are  
119 mediators for the weak interactions.  $W^\pm$  and  $Z^0$  bosons are massive while a photon and a gluon  
120 are massless particles.

121

122 The last SM particle is the Higgs boson. The Higgs boson is a scalar neutral particle which  
123 is playing a critical role in the electroweak symmetry breaking. The Higgs mechanism describes  
124 how  $W$  and  $Z$  bosons become massive particles.

125

126 All the particles are summarized in Fig. 1. These and only these fundamental particles and  
127 their antiparticles have been discovered by now. However, there are many composite particles  
128 which are called hadrons. Hadrons can consist of three quarks (baryons), quark and antiquark  
129 (meson), or three antiquarks (antibaryons). Hadrons always possess an integer charge.

130

131 Most of the particles are short-lived and decay within microseconds. The only stable parti-  
132 cles are protons and antiprotons, electrons and positrons, neutrinos and antineutrinos, photons,  
133 and, in some sense, gluons. However, if a particle cannot decay, it does not mean that it would  
134 live forever. There are many different kinds of reactions in which particles can disappear. An-  
135 tiprotons and positrons would immediately annihilate with protons and electrons, photons can  
136 be absorbed by charged particles, electrons and protons can scatter to produce neutrons and  
137 neutrinos and many other reactions are possible.

138

139 In this dissertation a process is studied where quark and antiquark interact to produce a  $W$   
140 boson which then decay as  $W^\pm \rightarrow e^\pm \nu_e (\bar{\nu}_e)$  or  $W^\pm \rightarrow \mu^\pm \nu_\mu (\bar{\nu}_\mu)$ . A photon is radiated off a  
141 quark or antiquark, a charged lepton or a  $W$  boson. The most interesting mechanism out of three  
142 is a radiation from a  $W$  boson because this is the triple gauge coupling where we potentially  
143 can have a new physics. Therefore, the focus of this study is an interaction between a photon

and a  $W$  boson however many other SM particles are relevant too. Thus, a charged lepton and a neutrino appear as the final state particles, a quark and an antiquark appear as initial state particles and all fundamental particles except the Higgs boson participate in various background processes. Subsections 1.2-1.4, chapter 2 and [1] describe particle interactions in more details.

148

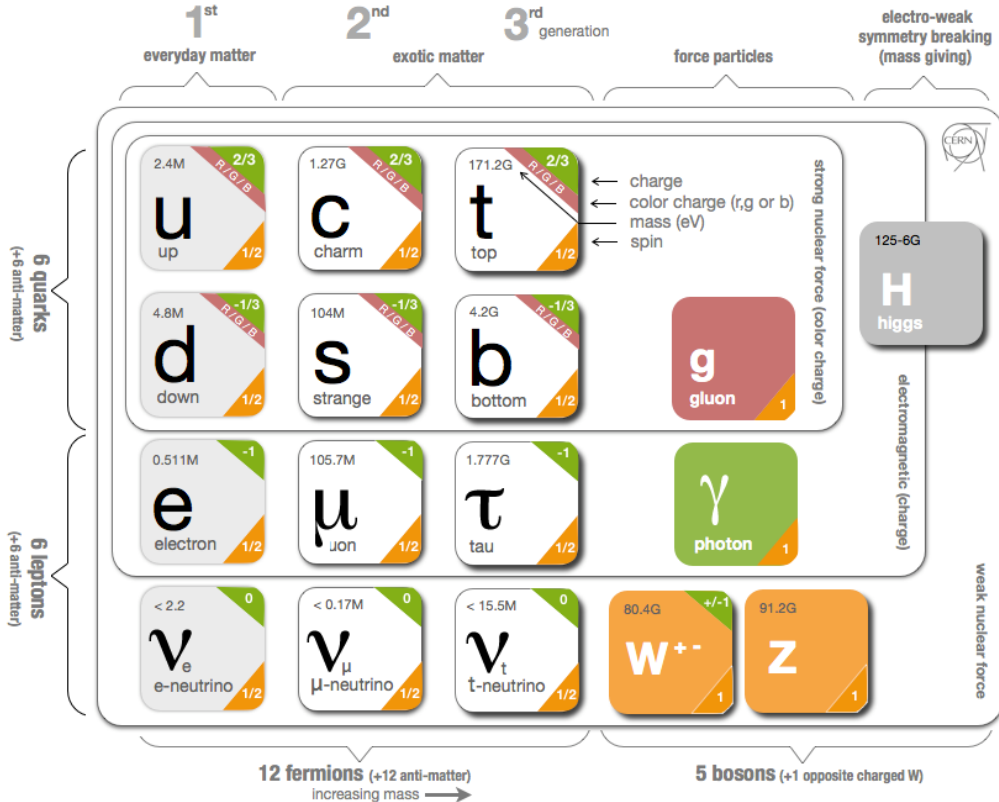


Figure 1: Standard Model Particles and Interactions. Source of the figure: [2].

<sup>149</sup> **1.2 Electroweak Interactions**

<sup>150</sup> All electrically charged particles participate in electromagnetic interactions. All electromagnetic  
<sup>151</sup> interactions are mediated by a photon, a spin-one electrically neutral massless particle, and can  
<sup>152</sup> be reduced to one elementary process (Fig. 2, left). This process represents a charged fermion  
<sup>153</sup> radiating or absorbing a photon. Such elementary process itself is forbidden by the energy con-  
<sup>154</sup> servation law but this element is a base of actual process. For example, the Bhabha scattering,  
<sup>155</sup>  $e^+e^- \rightarrow e^+e^-$ , occurs through  $e^+e^-$  annihilation with further production of a new  $e^+e^-$  pair  
<sup>156</sup> (Fig. 2, middle) or through exchange of a photon between the positron and the electron (Fig. 2,  
<sup>157</sup> right). Both cases involve nothing except the elementary process (Fig. 2, left). Such graphical  
<sup>158</sup> representations of the particle physics processes are called Feynman diagrams.

<sup>159</sup>

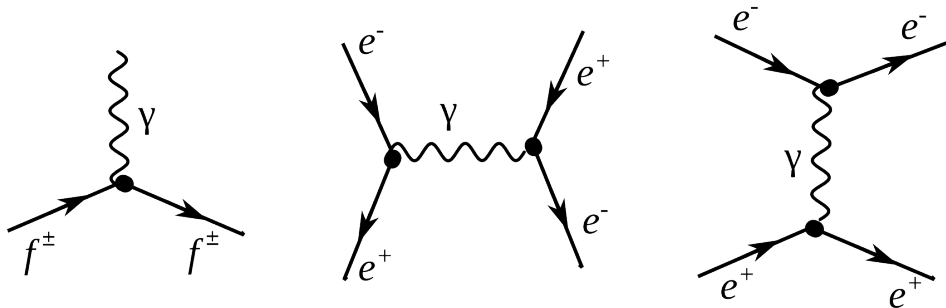


Figure 2: Electromagnetic interactions

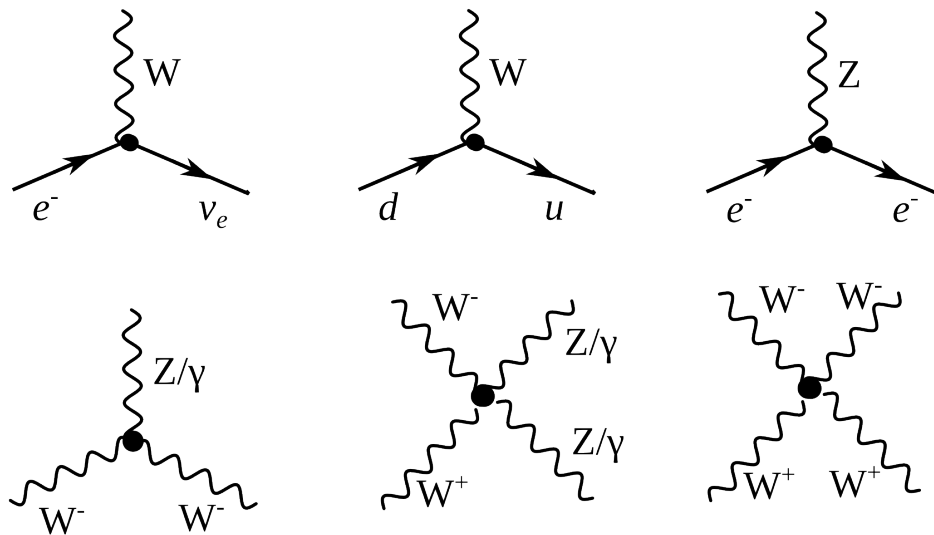


Figure 3: Weak elementary processes and gauge couplings

<sup>160</sup> As for the weak interactions, there are two kinds of them: neutral (mediated by a  $Z$  boson)

and charged (mediated by a  $W^\pm$  boson). Elementary processes with  $W$  and  $Z$  bosons are shown in Fig. 3. Because the electric charge must be conserved at any vertex, a particle radiating or absorbing a  $W$  boson converts to a different particle. Thus, a charged lepton converts to a neutrino (or vice versa) as shown in Fig. 3, top left. Each lepton carries a lepton flavor number (Tab. 1). A lepton flavor number is conserved in any interaction, thus an electron radiating a  $W$  boson always converts to an electron neutrino, a muon converts to a muon neutrino etc.

167

Table 1: Lepton Flavor Number

| particles                | $L_e$ | $L_\mu$ | $L_\tau$ |
|--------------------------|-------|---------|----------|
| $e^-, \nu_e$             | +1    | 0       | 0        |
| $e^+, \bar{\nu}_e$       | -1    | 0       | 0        |
| $\mu^-, \nu_\mu$         | 0     | +1      | 0        |
| $\mu^+, \bar{\nu}_\mu$   | 0     | -1      | 0        |
| $\tau^-, \nu_\tau$       | 0     | 0       | +1       |
| $\tau^+, \bar{\nu}_\tau$ | 0     | 0       | -1       |

From top middle diagram in Fig. 3 we see that if a quark with  $Q=-1/3$  enters, then a quark with  $Q=+2/3$  escapes and, therefore, the flavor of the quark is changed. The charged weak interaction is the only interaction which changes a quark flavor. The probability of each of three quarks with  $Q=+2/3$  to be born is determined by the Cabibbo-Kobayashi-Maskawa matrix which relates mass eigenstates  $d, c$  and  $b$  to weak eigenstates  $d', c'$  and  $b'$  (Eq. 1). Absolute values of the matrix elements are all known (Eq. 2) and are the highest for the quark of the same generation as an initial state quark. In the particular case shown in the top middle diagram in Fig. 3,  $d$  is the initial state quark and  $u$  has the highest probability to be produced after an interaction with a  $W$  boson but  $c$  and  $t$  can also be produced if there is enough energy.

177

$$\begin{pmatrix} d' \\ s' \\ b' \end{pmatrix} = \begin{pmatrix} V_{ud} & V_{us} & V_{ub} \\ V_{cd} & V_{cs} & V_{cb} \\ V_{td} & V_{ts} & V_{tb} \end{pmatrix} \begin{pmatrix} d \\ s \\ b \end{pmatrix} \quad (1)$$

$$\begin{pmatrix} |V_{ud}| & |V_{us}| & |V_{ub}| \\ |V_{cd}| & |V_{cs}| & |V_{cb}| \\ |V_{td}| & |V_{ts}| & |V_{tb}| \end{pmatrix} = \begin{pmatrix} 0.97 & 0.23 & 0.00 \\ 0.23 & 0.97 & 0.04 \\ 0.01 & 0.04 & 1.00 \end{pmatrix} \quad (2)$$

An elementary process of a neutral weak interaction is an emission of a  $Z$  boson off a fermion line (right top diagram in Fig. 3). An electron is shown here as an example however it could also be any lepton, antilepton, quark or antiquark. Diagrams with a  $Z$  boson are very similar to ones with a photon except a photon can only be radiated off a charged particle but a  $Z$  boson can also be radiated off a neutrino or antineutrino.

183

The bottom diagrams in Fig. 3 are gauge bosons coupling diagrams including self-coupling of a  $W$  boson, its interaction with a  $Z$  boson and its electromagnetic radiation of a photon. Charge-conserving triple and quartic gauge couplings containing two or four  $W$  bosons are all possible in the SM:  $WWZ$ ,  $WW\gamma$ ,  $WWZZ$ ,  $WWZ\gamma$ ,  $WW\gamma\gamma$ , and  $WWWW$ .

188

Electromagnetic and weak interactions are unified by the electroweak Glashow-Weinberg-Salam (GWS) theory which is based on  $SU(2) \times U(1)$  symmetry.  $SU(2)$  is the symmetry of weak isospin which generates three bosons:  $W^1$ ,  $W^2$  and  $W^3$ .  $U(1)$  is the symmetry of the weak

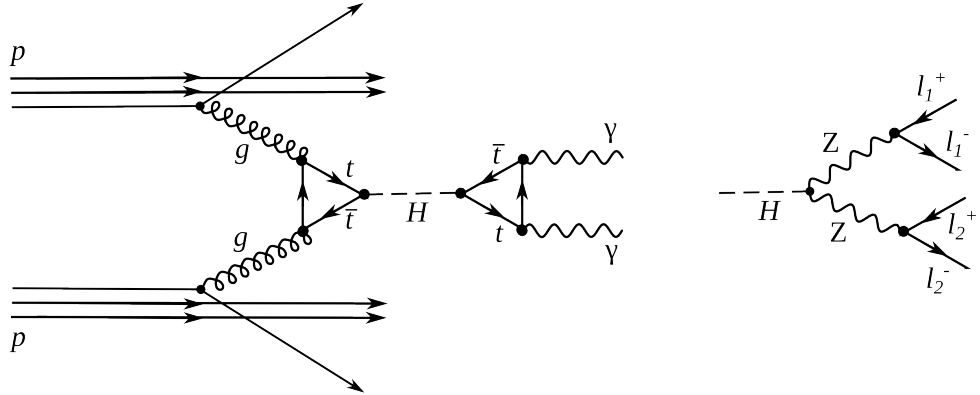


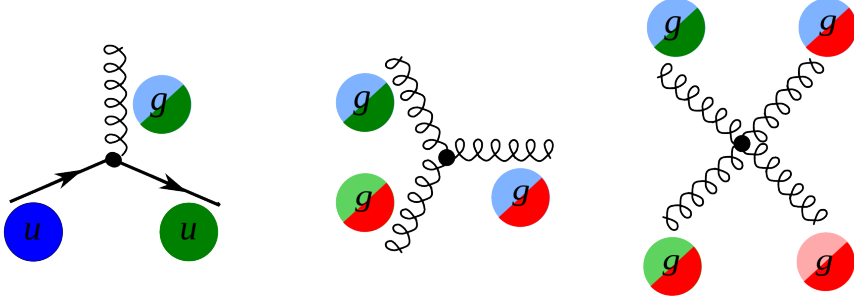
Figure 4: The Higgs boson production and decay

hypercharge and generate one neutral boson  $B$ .  $W^1$  and  $W^2$  are mixed to create  $W^+$  and  $W^-$  mediators while  $W^3$  and  $B$  are mixed to create a  $Z$  boson and a photon. Therefore, the GWS theory considers electromagnetic and weak forces as different manifestations of the electroweak force. The electroweak theory is discussed in greater details in Ch. 2.

However, weak interactions are mediated by heavy bosons ( $M_W = 80$  GeV,  $M_Z = 91$  GeV) while electromagnetic interactions are mediated by a massless photon, thus, the electroweak symmetry is broken. To explain this phenomenon, the Higgs mechanism was introduced. The mechanism predicted an existence of an additional boson: the Higgs boson. The Higgs boson was a missing piece of the SM for many years and was finally discovered in 2012 at LHC by ATLAS and CMS collaborations through the processes shown in Fig.4 [3], [4].

The measurement in this dissertation is an electroweak measurement because the process involves a  $W$  boson. It includes an interaction of a  $W$  boson with leptons and quarks as well as the triple gauge coupling  $WW\gamma$ . Thus, the measurement is a good test of the SM electroweak theory.

---

 208 **1.3 Strong Interactions**


213 Figure 5: Elementary processes of strong interactions

209 The third fundamental force after the electromagnetic and weak ones is the strong force. The  
 210 strong force is responsible for glueing protons and neutrons together in the nuclei as well as for  
 211 forming protons and neutrons themselves. The strong interactions occur by exchanging gluons  
 212 which are spin-one massless electrically neutral particles.

213  
 214 The elementary strong processes are shown in Fig. 5. There are three elementary processes:  
 215  $qqg$ ,  $ggg$  and  $gggg$ , all are involving particles with color charges. Thus, gluons couple to quarks  
 216 and self-couple. Color charges must be conserved at each elementary process of the strong inter-  
 217 action. Each quark possesses one of three colors at a time, and there are eight types of gluons  
 218 to cover all possible color exchanges.

219  
 220 The coupling constant of the strong interaction depends on a distance between interacting  
 221 particles: it becomes larger as the distance becomes larger. This property leads to two conse-  
 222 quences specific to the strong force: the confinement and the asymptotic freedom.

223  
 224 The asymptotic freedom means that when quarks are very close to each other they almost  
 225 do not interact with each other and therefore they are free. The confinement is the property  
 226 of quarks to always stay in the color neutral combinations (hadrons), it forbids the existence of  
 227 free quarks. A combination becomes color neutral when there is the same amount of color and  
 228 anticolor or if there is the same amount of each of the three colors. Thus, mesons are comprised  
 229 of a quark and an antiquark with the opposite color charges, and baryons are comprised of three  
 230 quarks: red, green and blue one. Examples of baryons include such well-known particles as a  
 231 proton and a neutron.

232  
 233 The strong interactions can be described by the QCD which is a quantum field theory in-  
 234 variant under  $SU(3)$  color transformations. When the distance between quarks is small which  
 235 corresponds to high energy, and thus the coupling constant  $\alpha_s \ll 1$  is small, the perturbative  
 236 approach can be used to compute observables.

237  
 238 The  $W\gamma$  process being measured in this dissertation is not intended to test QCD, but a good  
 239 understanding of QCD is essential for performing this measurement because the QCD corrections  
 240 to the Feynman diagrams of the process are large and has to be taken into account in produc-  
 241 ing simulation. In addition, QCD describes the dynamics of quarks and gluons within colliding  
 242 protons and predicts probabilities of one or another quark-antiquark pair to interact. Physics of  
 243 proton-proton collisions is discussed in the subsection 1.4.

244

## 1.4 Physics of Proton-Proton Collisions

Consider a  $pp$  collision at LHC. The proton energies are so high that each proton behaves as a complex structure. A proton is a baryon, it consists of three quarks:  $uud$ . These three quarks are called valence quarks. They interact with each other by exchanging gluons which produce virtual  $q\bar{q}$  pairs (Fig. 6). Such quarks are called sea quarks.

Any parton from one proton can interact with any parton from another proton. Probabilities  $f_i(x, Q^2)$  of any particular constituent  $i$  to interact are described partially by QCD and partially by experimental measurements and depend on the momentum transfer  $Q$  and the momentum fraction of a specific parton  $x$ . These probabilities are called parton distribution functions (PDFs).

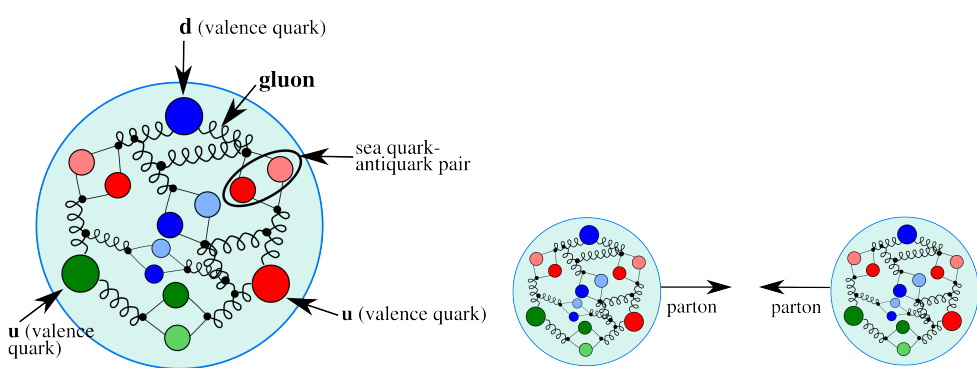


Figure 6: The proton structure (left) and the proton-proton collision (right).

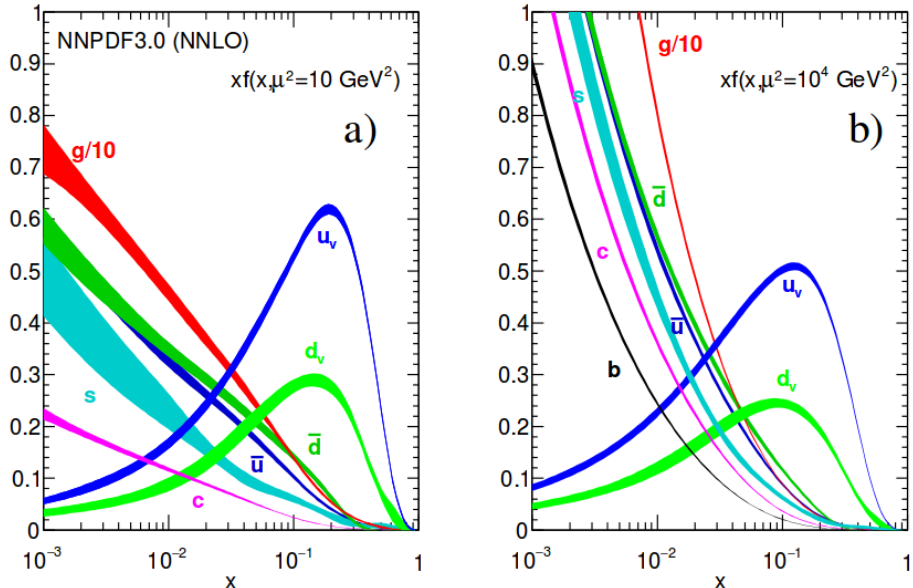


Figure 7: Parton distribution functions [5].

For large  $Q^2$  and  $x$  gluon-gluon interactions have the largest probabilities to occur (Fig. 7).

258 However, gluons do not couple directly to a  $W$  boson, thus, in the  $W\gamma$  measurement we are  
259 mostly interested in quark-antiquark pairs which would have a total charge corresponding to the  
260 charge of a  $W$  boson ( $\pm 1$ ). Since we have  $u$  and  $d$  as valence quarks and we know that the  
261 probability to couple to the same generation quark in charged weak interactions is the highest,  
262 most of the  $W$  bosons are created by  $u\bar{d}$  and  $d\bar{u}$  pairs however other  $q\bar{q}'$  combinations with the  
263 total charges of  $\pm 1$  are also possible. The antiquarks come from virtual  $q\bar{q}$  pairs inside of each  
264 proton.

265  
266 As we look for events containing  $W\gamma$  we also have other events mimicking our process. Such  
267 background events can be produced by any pair of partons.  
268

## 269 1.5 Open Questions of the Standard Model

270 While the SM is an accurate description of all particle physics experimental results, there are  
271 certain phenomena which are not included into the SM. In this subsection we discuss some of  
272 them.

273 The gravitational interactions do not fit into the SM. It is the open question whether the  
274 quantum theory of gravity is possible and whether there is a mediator of the gravitational in-  
275 teractions. Also, it is not known why the gravitational force is so much weaker than any other  
276 force. One possible explanation comes from a theory which predicts extra spatial dimensions  
277 beyond the three we are dealing with (e.g. the string theory). In this case, it is possible that the  
278 gravitational force is shared with other dimensions and that is why the fraction available in our  
279 three dimensions is that small.

281 Another mystery of the Universe is its composition: it is known from the studies of the grav-  
282 itational effects that our Universe consists of dark energy by 68%, of dark matter by 27% and of  
283 baryon matter only by 5% [?]. The dark energy resists the gravitational attraction and acceler-  
284 ates the expansion of the Universe, and is not detectable by any effects except gravitational. The  
285 understanding of the dark energy is a question of the general relativity rather than the particle  
286 physics. The dark matter however likely consists of particles and therefore is a subject of the  
287 particle physics. It does not radiate and that is why it cannot be detected by telescopes. The  
288 nature of the dark matter is not known but its constituents must be very stable to remain since  
289 the Big Bang. The theory of the supersymmetry which is unifying fundamental particles and  
290 mediators predicts many of new heavy particles and the lightest supersymmetric particle, the  
291 neutralino, is a good candidate for the dark matter.

293 One more open question is the reason for the matter/antimatter asymmetry. The matter  
294 and antimatter should have been created in the same amount at the moment of the Big Bang.  
295 Then most of it has annihilated but because of asymmetry, there was more matter than anti-  
296 matter which led to the state of the Universe we observe now. There is a phenomenon of  
297 the CP-violation in weak interactions observed and described that predicts the asymmetry at  
298 a certain level. However, the effect of the CP-violation is not large enough to account for the  
299 observed amount of the matter and, therefore, the total matter/antimatter asymmetry remains  
300 unexplained.

302 The measurement of the photon transverse momentum spectrum ( $P_T^\gamma$ ) of the  $W\gamma$  process has  
303 a goal to both test the SM and search for the BSM physics. The low  $P_T^\gamma$  region is not expected to  
304 be affected by any new physics and must agree well with the SM predictions while the high  $P_T^\gamma$   
305 region may indicate an existence of a new physics if there is an enhance over the SM predictions.  
306 The enhance would be an indirect evidence of the BSM particles like supersymmetric particles,  
307 additional gauge bosons or higher generation fermions. More theoretical details about the SM  
308 descriprion of  $W\gamma$  process as well as the possible BSM physics are given in the chapter 2.

<sub>311</sub> **2 W $\gamma$  Production Theory and Former Experimental Re-**

<sub>312</sub> **sults**

## 313 2.1 Electroweak Theory of the Standard Model

314 To develop a quantum field theory, we start with the Lagrangian of free fermions. In order  
315 to describe a system with a conservation of a physical quantity, the Lagrangian is required to  
316 satisfy a local invariance with respect to a certain transformation. For instance, a conservation  
317 of an electric charge requires a local invariance under  $U(1)$  transformation for the QED La-  
318 grangian [6]. The requirement of the local invariance introduces an interaction of a new vector  
319 field (or several fields) with our free fermions. The new vector field is a mediator of an inter-  
320 action conserving the physical quantity. To provide a full description for a new boson field, in  
321 addition to the interaction term we introduce an invariant term for the kinetic energy of the bo-  
322 son. Such approach allows us to derive the Lagrangian which is locally invariant with respect to  
323 a certain gauge transformation and contains interacting fermions as well as interaction mediators.  
324

325 The SM is a quantum field theory invariant under the local  $SU(3)_C \times SU(2)_L \times U(1)_Y$  trans-  
326 formation [6]. The SM Lagrangian includes all observed quantum fields and their interactions.  
327

328 The part of the SM Lagrangian based on the  $SU(3)_C$  symmetry and is called QCD or theory  
329 of strong interactions. QCD has three types of charges which are called colors: red, blue, and  
330 green. To be a subject of strong interaction, a fermion must posses a color charge. Quarks  
331 and antiquarks are such fermions. The requirement to satisfy the gauge invariance with respect  
332 to  $SU(3)_C$  transformations generates eight massless gluons, and the non-abelian nature of the  
333  $SU(3)$  group generates self-interactions of gluons including three-gluon and four-gluon vertices.  
334

335 The part of the SM Lagrangian based on the  $SU(2)_L \times U(1)_Y$  symmetry is a foundation of the  
336 unified theory of electroweak interactions.  $SU(2)_L$  reflects transformations in the weak isospin  
337 space of left-handed fermions ([1], Ch. 9) while  $U(1)_Y$  reflects transformations in a weak hyper-  
338 charge space of all fermions. The requirement of the local gauge invariant generates four massless  
339 vector bosons which are mediators of electromagnetic and weak interactions. The non-abelian  
340 structure of  $SU(2)$  group generates gauge boson couplings the same way as self-interactions of  
341 gluons appear in QCD.

342 Mass terms for the vector bosons would violate the gauge invariance of the electroweak La-  
343 grangian, however it is experimentally known that mediators of weak interactions are heavy  
344 particles with masses  $M_W = 80$  GeV and  $M_Z = 91$  GeV. A possible solution of the discrepancy  
345 is a mechanism of the spontaneous symmetry breaking. QED symmetry group  $U(1)$  remains  
346 unbroken because a photon is massless.  
347

349 The mechanism of the Spontaneous Symmetry Breaking and the appearance of the mass  
350 terms for  $W$  and  $Z$  boson is realized by introducing an additional doublet of scalar fields. After  
351 that, the Lagrangian is being transformed in such a way that  $W$  and  $Z$  bosons acquire masses  
352 through their interactions with a new particle: a Higgs boson ( $H$ ). A photon does not couple to  
353 the Higgs boson remaining a massless particle and keeping  $U(1)_{QED}$  symmetry unbroken.  
354

355 The measurement in this dissertation provides a test for the electroweak sector of the SM. We  
356 will retrace the steps of the derivation of the EWK part of the SM Lagrangian starting from terms  
357 of free fermions. The resulting Lagrangian accommodates electroweak gauge bosons including  
358 their self-couplings. One of these self-couplings,  $WW\gamma$ , is the primary focus of our measurement.  
359

360 It is experimentally known that dynamics of weak interactions depends on particle's chirality  
361 ([1], Ch. 4.4.1). In particular, a  $W$  boson couples to left-handed fermions and right-handed an-  
362 tifermions only. A  $Z$  boson couples to both left-handed and right-handed charged fermions and  
363 antifermions but only to left-handed neutrinos and right-handed antineutrinos. Given different  
364 properties of left-handed and right-handed fermions, they are treated differently by the elec-  
365 troweak theory.  $SU(2)$  doublets are introduced for the wave functions of left-handed fermions  
366 while  $SU(2)$  singlets are introduced for the wave functions of right-handed fermions. Equa-  
367 tions 3 and 4 show wave functions for the first generation fermions. Wave functions for the other

<sup>368</sup> two generations are constructed the same way.

<sup>369</sup>

$$\psi_1(x) = \begin{pmatrix} u \\ d' \end{pmatrix}_L, \psi_2(x) = u_R, \psi_3(x) = d'_R. \quad (3)$$

$$\psi_1(x) = \begin{pmatrix} \nu_e \\ e^- \end{pmatrix}_L, \psi_2(x) = \nu_{eR}, \psi_3(x) = e^-_R. \quad (4)$$

<sup>370</sup> The state  $d'$  in Eq. 3 is a mixture of  $d$ ,  $c$  and  $b$  quark's wave functions and is determined by the  
<sup>371</sup> quark mixing matrix which is also called Cabibbo-Kobayashi-Maskawa matrix [6]:

<sup>372</sup>

$$\begin{pmatrix} d' \\ c' \\ b' \end{pmatrix} = V \begin{pmatrix} d \\ c \\ b \end{pmatrix} \quad (5)$$

<sup>373</sup> To derive the unified electroweak Lagrangian, we start with the free fermion terms:

<sup>374</sup>

$$L_0 = \sum_{j=1}^3 i\bar{\psi}_j(x)\gamma^\mu\partial_\mu\psi_j(x), \quad (6)$$

<sup>375</sup> where  $\gamma^\mu$  are Dirac matrices ([1], Ch. 7.1) and  $\psi_j(x)$  are wave functions determined by Eqs. 3 and 4.

<sup>376</sup>

<sup>377</sup> The wave function  $\psi_1$  changes under the  $SU(2)_L \times U(1)_Y$  transformations in the following  
<sup>378</sup> way:

<sup>379</sup>

$$\psi_1(x) \rightarrow e^{iy_1\beta}U_L\psi_1(x), \quad (7)$$

<sup>380</sup> while the wave functions  $\psi_{(2,3)}(x)$  are singlets of  $SU(2)_L$  and are affected only by  $U(1)$  transfor-  
<sup>381</sup> mations:

<sup>382</sup>

$$eq : psi23_t ransform \psi_{(2,3)}(x) \rightarrow e^{iy_{(2,3)}\beta}\psi_{(2,3)}(x). \quad (8)$$

<sup>383</sup> The transformation in the weak isospin space is defined as  $U_L \equiv e^{i\sigma_i\alpha_i/2}$  where  $\sigma_i$  are Pauli  
<sup>384</sup> matrices ([1], Ch. 4.2.2). Phases  $\alpha_i(x)$  and  $\beta(x)$  in Eqs. 7 and ?? are arbitrary functions of  $x$ ,  
<sup>385</sup> and  $y_{(1,2,3)}$  are weak hypercharges which are named analogous to electric charges in QED.

<sup>386</sup>

<sup>387</sup> In order to satisfy the local  $SU(2)_L \times U(1)_Y$  invariance, partial derivatives in Eq. 6 have to  
<sup>388</sup> be substituted with covariant derivatives:

<sup>389</sup>

$$D_\mu\psi_1(x) = [\partial_\mu - ig\tilde{W}_\mu(x) - ig'y_1B_\mu(x)]\psi_1(x) \quad (9)$$

$$D_\mu\psi_{(2,3)}(x) = [\partial_\mu - ig'y_{(2,3)}B_\mu(x)]\psi_{(2,3)}(x) \quad (10)$$

<sup>390</sup> where  $g$ ,  $g'$  are arbitrary constants,

<sup>391</sup>

$$\tilde{W}_\mu(x) \equiv \frac{\sigma_i}{2}W_\mu^i(x) = \frac{1}{\sqrt{2}} \begin{pmatrix} \sqrt{2}W_\mu^3 & (W_\mu^1 - iW_\mu^2)/\sqrt{2} \\ ((W_\mu^1 + iW_\mu^2)/\sqrt{2} & -W_\mu^3 \end{pmatrix}, \quad (11)$$

<sup>392</sup>  $B_\mu$ ,  $W_\mu^1$ ,  $W_\mu^2$ ,  $W_\mu^3$  are four vector bosons that arise from the requirement of the Lagrangian to  
<sup>393</sup> be invariant under local  $SU(2)_L \times U(1)$  transformations.

<sup>394</sup>

395 The Lagrangian becomes:

396

$$L_0 \rightarrow L = \sum_{j=1}^3 i\bar{\psi}_j(x)\gamma^\mu D_\mu \psi_j(x) \quad (12)$$

397 To make new vector bosons physical fields it is necessary to add terms for their kinetic energies:

398

$$L_{KIN} = -\frac{1}{4}B_{\mu\nu}B^{\mu\nu} - \frac{1}{4}W_{\mu\nu}^i W_i^{\mu\nu} \quad (13)$$

399 where  $B_{\mu\nu} \equiv \partial_\mu B_\nu - \partial_\nu B_\mu$ ,  $W_{\mu\nu}^i \equiv \partial_\mu W_\nu^i - \partial_\nu W_\mu^i + g\epsilon^{ijk}W_\mu^j W_\nu^k$

400

401 Off-diagonal terms of  $\tilde{W}_\mu$  are wave functions of charged vector bosons  $W^\pm = (W_\mu^1 \mp iW_\mu^2)/\sqrt{2}$   
402 while  $W_\mu^3$  and  $B_\mu$  are neutral fields which are mixtures of a  $Z$  boson and a photon determined by:  
403

$$\begin{pmatrix} W_\mu^3 \\ B_\mu \end{pmatrix} \equiv \begin{pmatrix} \cos\theta_W & \sin\theta_W \\ -\sin\theta_W & \cos\theta_W \end{pmatrix} \begin{pmatrix} Z_\mu \\ A_\mu \end{pmatrix} \quad (14)$$

404 where  $\theta_W$  is an electroweak mixing angle,  $A_\mu$  is a photon field.

405

406 In order to be consistent with QED, terms involving  $A_\mu$  in the electroweak Lagrangian must  
407 be equal to the corresponding terms in QED Lagrangian [6]:  
408

$$L_{QED} = i\bar{\psi}(x)\gamma^\mu \partial_\mu \psi(x) - m\bar{\psi}(x)\psi(x) + qA_\mu(x)\bar{\psi}(x)\gamma^\mu \psi(x) - \frac{1}{4}F_{\mu\nu}(x)F^{\mu\nu}(x), \quad (15)$$

409 where  $q$  is electric charge of  $\psi(x)$  field,  $F_{\mu\nu} \equiv \partial_\mu A_\nu - \partial_\nu A_\mu$ .

410

411 This requirement relates  $g$ ,  $g'$ ,  $\theta_W$  and  $e$  as  $g \sin\theta_W = g' \cos\theta_W = e$  and provides expression  
412 for weak hypercharges:  $y = q - t_3$ , where  $q$  is the electric charge and  $t_3$  is a  $z$ -component of the  
413 weak isospin. This results in  $y_1 = 1/6$ ,  $y_2 = 2/3$ , and  $y_3 = -1/3$  for quarks and  $y_1 = -1/2$ ,  
414  $y_2 = 0$ , and  $y_3 = -1$  for leptons. A right-handed neutrino has a weak hypercharge of  $y_2 = 0$ . It  
415 also does not have an electric charge and, as a right-handed fermion, has  $t_3 = 0$  and, therefore,  
416 does not couple to a  $W$  boson. Thus, a right-handed neutrino does not participate in any SM  
417 interaction.

418

419 Writing  $\tilde{W}_\mu$  in Eq. 13 explicitly, we obtain TGC and QGC coupling terms:  
420

$$L_{TGC} = -\frac{g}{4}(\partial_\mu W_\nu^i - \partial_\nu W_\mu^i)\epsilon^{ijk}W^{\mu j}W^{\nu k} - \frac{g}{4}\epsilon^{ijk}W_\mu^j W_\nu^k(\partial^\mu W^{\nu i} - \partial^\nu W^{\mu i}) \quad (16)$$

$$L_{QGC} = -\frac{g^2}{4}\epsilon^{ijk}\epsilon^{ilm}W_\mu^j W_\nu^k W^{\mu l}W^{\nu m} \quad (17)$$

421 Substituting  $W_\mu^i$  and  $B_\mu$  in Eq. 16 and Eq. 17 with the wave functions of  $W^\pm$ ,  $Z$  and a photon:  
422

$$B_\mu = -\sin\theta_W Z_\mu + \cos\theta_W A_\mu, \quad W_\mu^3 = \cos\theta_W Z_\mu + \sin\theta_W A_\mu, \quad (18)$$

$$W_\mu^1 = \sqrt{2}(W^+ + W^-), \quad W_\mu^2 = \sqrt{2}(W^- + W^+), \quad (19)$$

423 we receive charged TGC and QGC Lagrangians in the forms of Eqs. 20 and 23.

424

425 Equation 20 involves  $WWZ$  (Eq. 21) and  $WW\gamma$  (Eq. 22) interactions:  
426

$$L_{TGC} = L_{TGC}^{(1)} + L_{TGC}^{(2)}, \quad (20)$$

$$L_{TGC}^{(1)} = -ie \cot \theta_W (W^{-\mu\nu} W_\mu^+ Z_\nu - W^{+\mu\nu} W_\mu^- Z_\nu + W_\mu^- W_\nu^+ Z^{\mu\nu}), \quad (21)$$

$$L_{TGC}^{(2)} = -ie (W^{-\mu\nu} W_\mu^+ A_\nu - W^{+\mu\nu} W_\mu^- A_\nu + W_\mu^- W_\nu^+ A^{\mu\nu}). \quad (22)$$

427     Equation 23 involves  $WWWW$  (Eq. 24),  $WWZZ$  (Eq. 25),  $WWZ\gamma$  (Eq. 26), and  $WW\gamma\gamma$   
428     (Eq. 27) interactions:

429

$$L_{QGC} = L_{QGC}^{(1)} + L_{QGC}^{(2)} + L_{QGC}^{(3)} + L_{QGC}^{(4)}, \quad (23)$$

$$L_{QGC}^{(1)} = -\frac{e^2}{2 \sin^2 \theta_W} (W_\mu^+ W^{-\mu} W_\nu^+ W^{-\nu} - W_\mu^+ W^{\mu} W_\nu^- W^{-\nu}), \quad (24)$$

$$L_{QGC}^{(2)} = -e^2 \cot^2 \theta_W (W_\mu^+ W^{-\mu} Z_\nu Z^\nu - W_\mu^+ Z^\mu W_\nu^- Z^\nu), \quad (25)$$

$$L_{QGC}^{(3)} = -e^2 \cot \theta_W (2W_\mu^+ W^{-\mu} Z_\nu A^\nu - W_\mu^+ Z^\mu W_\nu^- A^\nu - W_\mu^+ A^\mu W_\nu^- Z^\nu), \quad (26)$$

$$L_{QGC}^{(4)} = -e^2 (W_\mu^+ W^{-\mu} A_\nu A^\nu - W_\mu^+ A^\mu W_\nu^- A^\nu). \quad (27)$$

430     In the measurement of this dissertation we probe  $WW\gamma$  coupling (Eq. ??).

431

432     The unified electroweak Lagrangian discussed above involves kinetic energy terms for fermions  
433     and gauge bosons as well as interactions of fermions with gauge bosons, TGC, and QGC. How-  
434     ever, this Lagrangian does not contain any mass terms. Because left-handed and right-handed  
435     wave functions transform differently under the electroweak symmetry, adding fermion mass terms  
436     of  $\frac{1}{2}m_f^2 \bar{\psi}\psi$  would violate the Lagrangian invariance and, therefore, fermion mass terms are for-  
437     bidden by the  $SU(2) \times U(1)$  symmetry requirement. Mass terms for gauge bosons also would  
438     violate the Lagrangian invariance just as a photon mass term  $\frac{1}{2}m^2 A^\mu A_\mu$  would violate  $U(1)$   
439     invariance of  $L_{QED}$  [1]. Therefore, Lagrangian  $L$  in Eq. 12 contains massless particles only.

440

441     However, it is known from experiments that a  $Z$  boson, a  $W$  boson and fermions are massive  
442     particles and, therefore, our theory should accommodate their masses. To introduce masses into  
443     the electroweak Lagrangian, an  $SU(2)_L$  doublet of complex scalar fields  $\phi(x)$  is added to the  
444     Lagrangian:

445

$$\phi(x) \equiv \begin{pmatrix} \phi^{(+)}(x) \\ \phi^{(0)}(x) \end{pmatrix} \quad (28)$$

446     By selecting a special gauge of  $\phi(x)$  it is possible to spontaneously break electroweak sym-  
447     metry, generate a new scalar particle, a Higgs boson [6], and introduce mass terms for  $W$  and  
448      $Z$  bosons and charged fermions through their couplings to the Higgs boson. The strength of the  
449     coupling constant is proportional to the square of the particle's mass, therefore, heavier particles  
450     are more likely to interact with  $H$ , and massless particles do not couple to  $H$ .

451

452     The mechanism of generating a fermion's mass involves both left-handed and right-handed  
453     components of the fermion. If our hypothesis that right-handed neutrinos do not exist is right,  
454     then the Higgs mechanism does not generate neutrino masses. However, from the experiments  
455     of neutrino oscillations, neutrinos are known to have masses even though they are orders of  
456     magnitude smaller than those of other fermions. Several hypotheses were offered to resolve this  
457     contradiction however at the moment the mechanism of neutrinos to acquire masses remain un-  
458     known [5].

459

460 In this dissertation, we study an electroweak process  $W\gamma \rightarrow l\nu_l\gamma$ , more specifically, probe  
461 TGC vertex  $WW\gamma$  (Eq. 22). To do that, we are measuring a differential cross section with  
462 respect to the photon transverse momentum. The concept of the cross section in particle physics  
463 is discussed in the next chapter.

464

## 2.2 Cross Section and Luminosity

In this dissertation we are measuring the total and the differential cross section. The cross section in particle physics is the interaction probability per unit flux of incident particles [11]. It can be interpreted as area which must be crossed by an incident particle in order to interact with a scattering center, or, in case of a differential cross section, area  $d\sigma$  within which an incident particle must appear to be scattered off by an angle  $d\theta$  (Fig. 8). The relationship between  $d\sigma$  and  $d\theta$  gives us the expression for a differential cross section  $d\sigma/d\theta$ . Integrating over  $d\theta$ , one would get the total cross section  $\sigma$ .

In Fig. 8 an incident particle is the same as a final state particle, however in particle physics final state particles can differ from initial state particles, and we measure a differential cross section with respect to a parameter  $X$  of the final state particle. Differentiating  $\sigma$  by  $X$  we get the expression for the differential cross section  $d\sigma/dX$ .

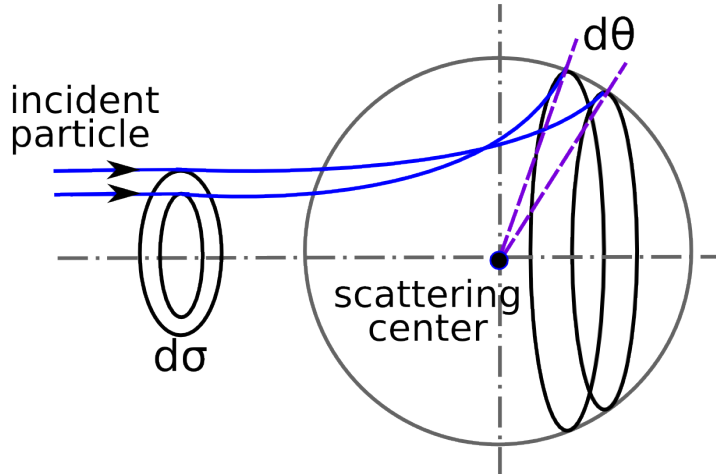


Figure 8: Illustration of the differential cross section concept in the classical case.

Referring to the Fig. 8, a number of particles passing through the area  $\sigma$  per unit time is  $N = L \cdot \sigma$ , where  $L$  is the flux of incident particles and is called luminosity. Therefore, the cross section  $\sigma$  of a specific process can be determined from an experiment as  $\sigma = N/L$ .

A cross section also can be computed theoretically. The formula to compute a cross section is:

$$\sigma = \frac{W_{fi}}{L} N_{fs}, \quad (29)$$

where  $W_{fi}$  is a transition probability between final and initial states of the system per unit volume,  $L$  is the flux of initial particles, and  $N_{fs}$  is the density of final states [7], Ch. 4.3.

The formula of the cross section is called the Fermi's Golden Rule [1]. In case of the scattering of two particles to three final state particles  $1 + 2 \rightarrow 3 + 4 + 5$ , it takes the following form:

$$\sigma = \frac{1}{4\sqrt{(p_1 p_2)^2 - (m_1 m_2)^2}} \int |M|^2 (2\pi)^4 \delta^4(p_1 + p_2 - p_3 - p_4 - p_5) \prod_{j=3}^5 \frac{1}{2\sqrt{\bar{p}_j^2 + m_j^2}} \frac{d^3 \bar{p}_j}{(2\pi)^3}, \quad (30)$$

491 where  $p_i$  are 4-momenta and  $\bar{p}_i$  are three momenta of the initial state and the final state  
492 particles,  $m_i$  are masses of particles,  $M$  is the process amplitude determined by the dynamics  
493 of the particles interaction. All available momenta of the final state particles is called the phase  
494 space.

495 The cross section of the hard scattering in proton-proton collisions  $pp \rightarrow X + Y$  has two  
496 ingridients: PDFs and a partonic cross section  $\sigma_{ab \rightarrow X}$ . The partonic cross section is described  
497 by perturbative QCD while PDFs require non-perturbative computations and are determined,  
498 in part, from experiments (Fig. 7). According to the QCD factorization theorem [8]:  
500

$$\sigma(pp \rightarrow X + Y) = \sum_{a,b} \int dx_a dx_b f_a(x_a, Q^2) f_b(x_b, Q^2) \sigma(ab \rightarrow X). \quad (31)$$

501 In case of  $W\gamma$  process,  $X$  is  $l\nu\gamma$ ,  $ab$  are  $q_i\bar{q}_j$  or  $q_j\bar{q}_i$ .  $Q^2$  is the large momentum scale that char-  
502 acterizes hard scattering,  $f_a$  and  $f_b$  are PDFs,  $x_a$  and  $x_b$  are fractions of momenta of the partons.  
503

### 2.3 Standard Model $W\gamma$ Production

A  $W$  boson in proton-proton collisions can be produced in the processes  $q\bar{q}' \rightarrow W$  where  $q$  and  $\bar{q}'$  are a quark and an antiquark which have a total charge of +1 if producing a  $W^+$  boson or of -1 if producing a  $W^-$  boson. The processes  $u\bar{d} \rightarrow W^+$  and  $d\bar{u} \rightarrow W^-$  are the most likely to occur because  $u$  and  $d$  are valence quarks in a proton. Antiquarks  $\bar{d}$  and  $\bar{u}$  come from sea  $q\bar{q}$  pairs of the other proton.

A  $W$  boson decays immediately after being created, and we do not detect the  $W$  boson itself but its decay products. Decay modes of a  $W$  boson include  $W^\pm \rightarrow l^\pm \nu_l (\bar{\nu}_l)$  where  $l^\pm = e^\pm, \mu^\pm$  or  $\tau^\pm$  with branching fractions of 11% per a leptonic channel [5]. The rest 67% stands for various  $W \rightarrow q\bar{q}'$  decays. In this dissertation we only consider  $W^\pm \rightarrow \mu^\pm \nu_\mu (\bar{\nu}_\mu)$  and  $W^\pm \rightarrow e^\pm \nu_e (\bar{\nu}_e)$  as the cleanest channels.

A photon can be emitted from any charged particle of the process: a quark, an antiquark, a charged lepton or a  $W$  boson (Fig. 9, top). A quark and an antiquark are initial state particles and, therefore, if one of them radiates a photon, we call such process the Initial State Radiation (ISR). A muon or an electron is a final state particle and if it radiates a photon, we call such process the Final State Radiation (FSR). Finally, a  $W$  boson is a gauge boson and if it radiates a photon, the process has a vertex with three gauge bosons:  $WW\gamma$ , and we call such process the Triple Gauge Coupling (TGC).

524

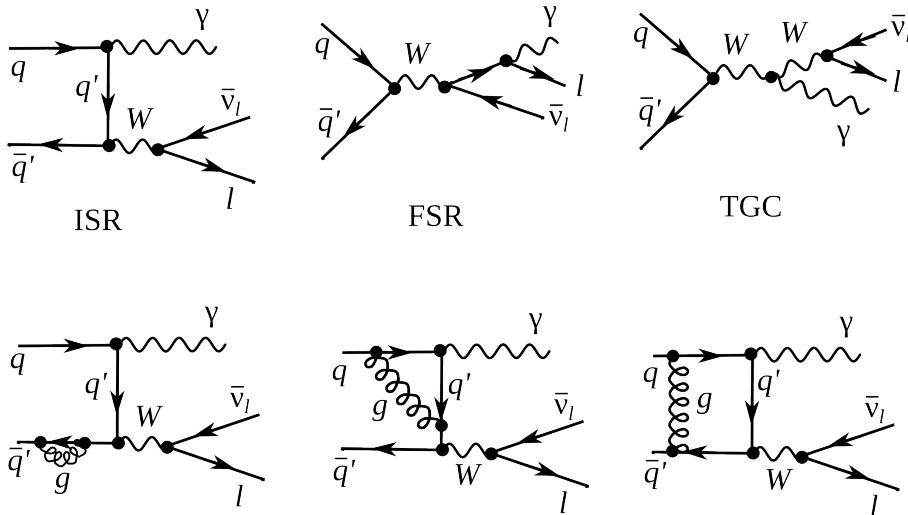


Figure 9: Feynman diagrams of  $W\gamma$  production

The electroweak Lagrangian is described in Chapter 2.1. It is possible to derive equations of motion from the Lagrangian for any fields involved [1]. However, in a quantum field theory equations of motion cannot be solved exactly and, therefore, the perturbative approach is used if coupling constants are  $g \ll 1$ .

529

To represent the process graphically Feynman diagrams were invented. Also the diagrams can be used to calculate the process amplitude  $M$  from Eq. 30 because they are determined by Lagrangian terms relevant to the process. There is infinite number of Feynman diagrams corresponding to any specific process and the total amplitude of the process is a sum of individual amplitudes of each diagram and it is not technically possible to take into account all of them.

530

531

532

533

534

535 The perturbative approach arranges all the diagrams by orders of contribution because each  
536 vertex is assigned a coupling constant and, therefore, the Feynman diagrams with fewer vertices  
537 would give a significantly larger contribution to the amplitude. In Fig. 9 we have examples of the  
538 Leading Order (LO) and the Next-to-Leading Order (NLO) Feynman diagrams (top and bottom  
539 diagrams respectively).

540

541 The  $W\gamma$  process is represented by four LO Feynman diagrams with three vertices each. The  
542  $W\gamma$  process amplitude and cross section are long, complicated expressions, therefore, they are not  
543 quoted in this dissertation. The first calculation of the  $W\gamma$  process with necessary formulas can  
544 be found in [13].

545

546 The NLO corrections shown in Fig. 9 are QCD corrections only which include gluon loops  
547 at the same quark line and exchange of a gluon between two different quark lines however QED  
548 and weak NLO diagrams are also possible. QED corrections mean radiations of extra photons  
549 by charged particles, exchange of photons between different charged particles or a photon can be  
550 radiated and absorbed by the same charged particle forming a loop. Similarly, weak corrections  
551 mean extra virtual  $W$  or  $Z$  bosons. But the QCD corrections are the largest.

552

553 The theoretical cross section in particle physics is important not only for analyzing the measurement  
554 result but also for producing the simulation which is then actively used while performing the measurement.  
555 The simulation consists of two parts: the generation of the process and the simulation of the particles paths through the detector. While the second one depends on the  
556 well-known properties of the particles and the detector configurations, the first part relies on the  
557 theory.

558

559 The most precise theoretical  $W\gamma$  cross section available is the Next-to-Next-to-Leading Order  
560 (NNLO) cross section in QCD [14]. The effect of the NNLO correction ranges from 19% to 26%  
561 compared to the NLO cross section depending on the selection conditions. The contributions  
562 from the higher order corrections is estimated to be  $\pm 4\%$ . However, the NNLO theoretical result  
563 was published in 2015 only and there is still no simulation available based on that result. The  
564 simulation used in this analysis is LO + up to two hadronic jets simulation which found to give  
565 the same predictions as the NLO result.

566

567 In addition to the SM predictions, there are certain BSM theories which predict an enhancement  
568 of the contribution from the TGC diagram. The discussion of these BSM effects and how  
569 they affect the  $W\gamma$  process takes place in Chapter 2.4.

570

## 2.4 Anomalous $W\gamma$ Production

Most BSM physics theories predict the existence of particles which are heavier than the discovered energy range. If their masses are not accessible even by the most energetic machines, the direct detection of such particles is not possible. However, they can contribute to the productions of lower energetic particles producing loops where such heavy particles would be off-shell. The loops would give additional contributions to the process amplitude and, therefore, there would be more events produced in the process than one can expect based on the SM predictions.

These effects can be probed by precision measurements of the SM processes. In the electroweak sector processes of such interest include diboson and triboson productions which can occur through triple gauge couplings and quartic gauge couplings.

Triple and quartic gauge couplings (QGC) are represented by vertices with three and four bosons (Fig. 10). As discussed in Chapter 2.1, charged TGC and QGC are possible at tree level in the SM while neutral TGC and QGC are not.

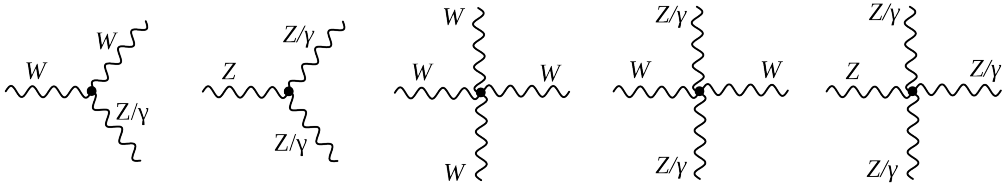


Figure 10: TGC and QGC vertices

To account for the effects from the potential loops of heavy particles, we introduce an effective Lagrangian with arbitrary values of coupling constants which can be shrunk to the SM Lagrangian if these constants would have their SM values. Such approach makes our searches model-independent because we do not specify which exactly particles form the loops but instead just check whether there is a deviation from the SM.

In  $W\gamma$  measurement we can probe  $WW\gamma$  vertex only. The most general Lorentz invariant Lagrangian of this vertex takes the following form [16]:

$$iL_{eff}^{WW\gamma} = iL_{eff(1)}^{WW\gamma} + iL_{eff(2)}^{WW\gamma} + iL_{eff(3)}^{WW\gamma} \quad (32)$$

$$iL_{eff(1)}^{WW\gamma} = e[g_1^\gamma A^\mu (W_{\mu\nu}^- W^{+\nu} - W_{\mu\nu}^+ W^{-\nu}) + \kappa_\gamma W_\mu^+ W_\nu^- A^{\mu\nu} + \frac{\lambda_\gamma}{m_W^2} A^{\mu\nu} W_\nu^{+\rho} W_{\rho\mu}^-] \quad (33)$$

$$iL_{eff(2)}^{WW\gamma} = e[i g_5^\gamma \epsilon_{\mu\nu\rho\sigma} ((\partial^\rho W^{-\mu}) W^{+\nu} - W^{-\mu} (\partial^\rho W^{+\nu})) V^\sigma + i g_4^\gamma W_\mu^- W_\nu^+ (\partial^\mu A^\nu + \partial^\nu A^\mu)] \quad (34)$$

$$iL_{eff(3)}^{WW\gamma} = e[\frac{\tilde{\kappa}_\gamma}{2} W_\mu^- W_\nu^+ \epsilon^{\mu\nu\rho\sigma} A_{\rho\sigma} - \frac{\tilde{\lambda}_\gamma}{2m_W^2} W_{\rho\mu}^- W_\nu^{+\mu} \epsilon^{\nu\rho\alpha\beta} A_{\alpha\beta}] \quad (35)$$

where  $e$  is the absolute value of the electron charge,  $A^\mu$  is the photon field,  $W^{\pm\mu}$  are fields of  $W^\pm$  bosons,  $W_{\mu\nu} = \partial_\mu W_\nu - \partial_\nu W_\mu$ ,  $A_{\mu\nu} = \partial_\mu A_\nu - \partial_\nu A_\mu$ ,  $m_W$  is the mass of a  $W$  boson,  $g_1^\gamma$ ,  $\kappa_\gamma$ ,  $\lambda_\gamma$ ,  $g_5^\gamma$ ,  $g_4^\gamma$ ,  $\tilde{\kappa}_\gamma$ , and  $\tilde{\lambda}_\gamma$  are constants.

601     Despite there are 7 constants in the extended Lagrangian, only  $\lambda_\gamma$  and  $\kappa_\gamma$  are considered  
 602     in the aTGC searches. The rest of the constants are fixed to their SM values based on various  
 603     considerations. Thus,  $g_1^\gamma = 1$  and  $g_5^\gamma = 0$  are fixed to obey the electromagnetic gauge invariance  
 604     for the on-shell photons. The non-zero value of  $g_5^\gamma$  also violates C and P conservations, and  
 605     non-zero values of  $g_4^\gamma$ ,  $\kappa_\gamma$ ,  $\tilde{\lambda}_\gamma$  violate the CP conservation law. Such violation parametrizations  
 606     are not considered in charged TGC measurements now but might get considered in the future.  
 607

608     The presence of aTGC would have larger effects at high energy scales. Fig. 11 shows these  
 609     effect in  $P_T^\gamma$  spectrum of 7 TeV  $W\gamma \rightarrow \mu\nu\gamma$  measurement. Fig. 12 shows the examples of these  
 610     effects in  $m_{ll}$  spectrum in 8 TeV  $WW \rightarrow l\nu l\nu$  measurement (left) and  $P_T^\gamma$  spectrum in 7 TeV  
 611      $Z\gamma \rightarrow \nu\nu\gamma$  measurement (right). It is seen on the plots that aTGC spectrum at low  $m_{ll}$  or low  
 612      $P_T^\gamma$  coincides with the SM prediction but for higher  $m_{ll}$  or  $P_T^\gamma$  the disagreement becomes more  
 613     significant.  
 614

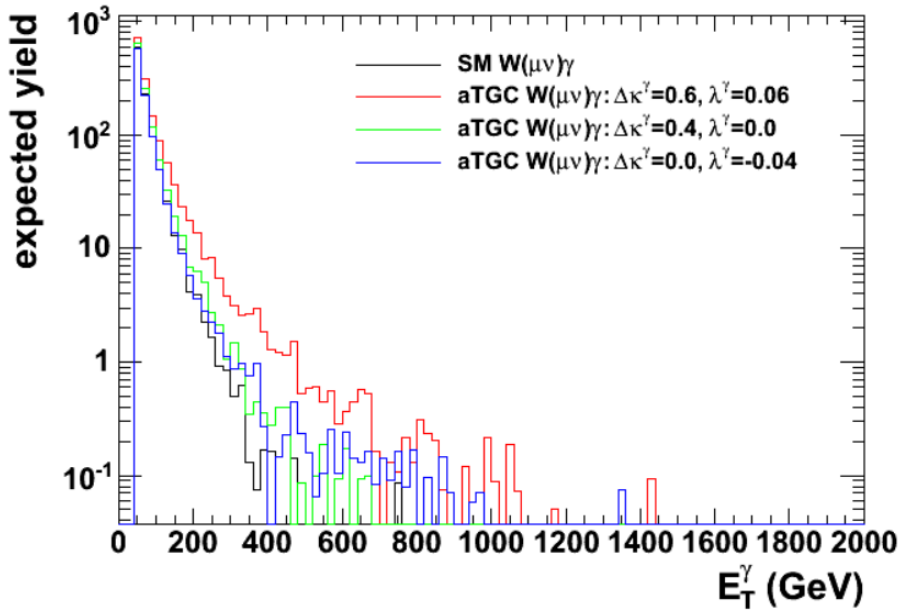


Figure 11: Distributions of  $P_T^\gamma$  of simulated  $W\gamma \rightarrow \mu\nu\gamma$  events with different values of aTGC constants at LHC energy of  $\sqrt{s} = 7$  TeV. Source of figure: [17].

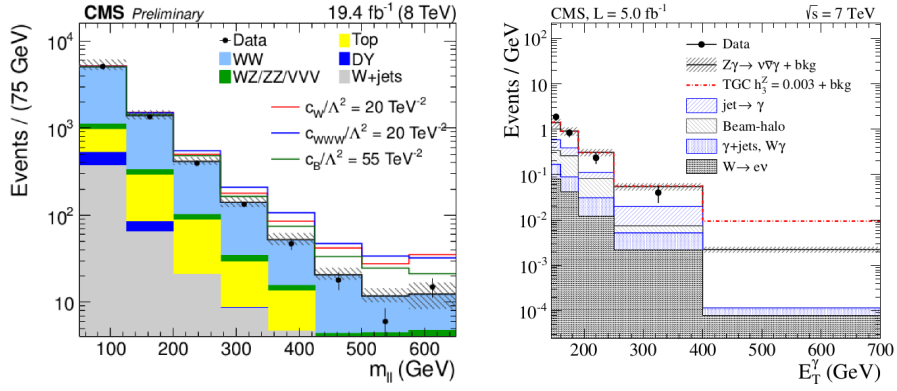


Figure 12: Examples of the potential effects of non-zero TGC constants in  $m_{ll}$  spectrum in 8 TeV  $WW \rightarrow l\nu l\nu$  measurement (left) [28] and  $P_T^\gamma$  spectrum in 7 TeV  $Z\gamma \rightarrow \nu\nu\gamma$  measurement (right) [29].

## 2.5 Measurements in the Past

ATGC parameters of  $WW\gamma$  vertex can be probed in  $W\gamma$ ,  $WW$ , and  $WZ$  measurements. Limits on  $\Delta\kappa_\gamma$  and  $\lambda_\gamma$  constants from different D0 [18], LEP [19], ATLAS [20], [21], [22] and CMS [24], [25], [26], [27] measurements are summarized in Fig. 13.

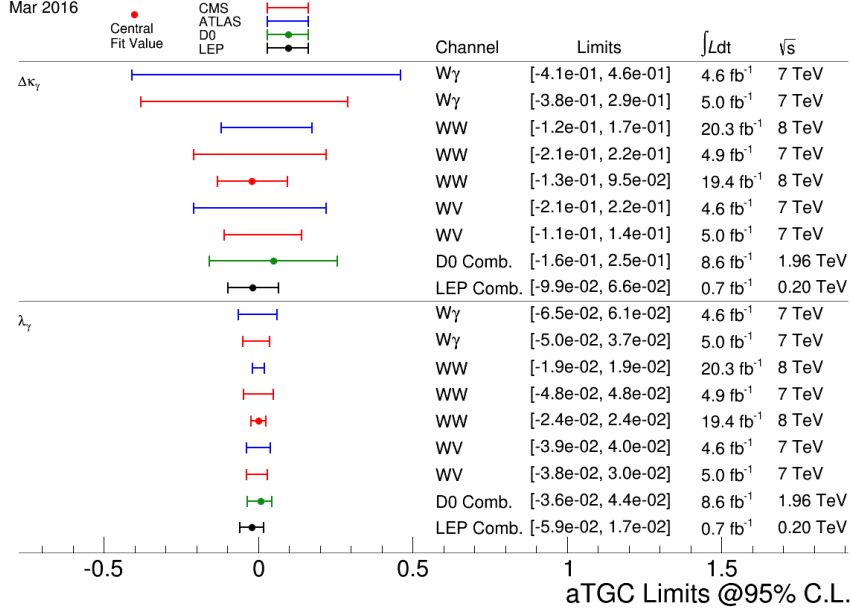


Figure 13: Summary of limits on the  $WW\gamma$  aTGC coupling constants. Figure from [23]

The most recent measurements of  $W\gamma$  production were performed by CMS [24] and ATLAS [20] collaborations with  $pp$  collisions at  $\sqrt{s} = 7$  GeV collected in 2011. The measurements are based on  $5 \text{ fb}^{-1}$  and  $4.6 \text{ fb}^{-1}$  of integrated luminosity with CMS and ATLAS respectively. Both collaborations considered two channels:  $W\gamma \rightarrow \mu\nu\gamma$  and  $W\gamma \rightarrow e\nu\gamma$ .

Dibosons processes are rare in  $pp$ -collisions and we have to filter out events of our interest from many processes which are more likely to happen. To do that, we apply variety of selection criteria which reject most of background events increasing our signal rate as much as possible. However, even after we applied all possible selection criteria, majority of our selected events are still background events and it is not possible to reduce the background any further without also significantly reducing signal.

The major source of such irreducible background is the fake photon background where hadronic jets are misidentified as photons. Such events originate from  $W+\text{jets}$  process mostly but  $Z+\text{jets}$  and  $t\bar{t}+\text{jets}$  events contribute to this source of the background as well. The second major background for the electron channel is the fake photon background where electron can be misidentified as a photon. Such events are coming from  $Z+\text{jets}$  events. Other sources of backgrounds include real- $\gamma$  backgrounds, fake lepton + real photon and fake lepton + fake photon sources.

Both channels provide measurements of  $p_T^\gamma$  spectra because this variable is the most sensitive to the potential ATGC. The  $p_T^\gamma$  spectra of the selected events in data superimposed with selected events in the simulation of the signal and estimated background contribution for the muon and electron channels are shown in Fig. 14 for CMS and in Fig. 15 for ATLAS. Both measurements show a good agreement.

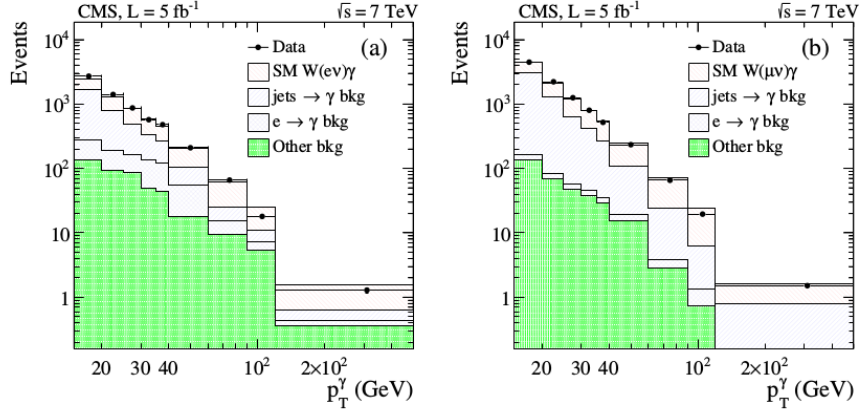


Figure 14: The distribution fo the  $p_T^\gamma$  of  $W\gamma$  candidates in the analysis of 7 TeV CMS data. Data vs signal MC + background estimates. Left:  $W\gamma \rightarrow e\nu\gamma$ , right:  $W\gamma \rightarrow \mu\nu\gamma$  [24].

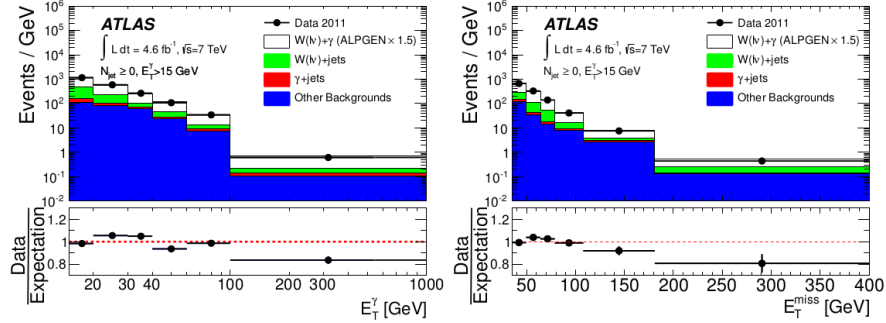


Figure 15: The distribution fo the  $p_T^\gamma$  (left) and  $E_T^\text{miss}$  (right) of  $W\gamma$  candidates in the analysis of 7 TeV ATLAS data. Data vs signal MC + background estimates [20].

CMS provides measurements of the  $P_T^\gamma$  spectrum, the total cross section within the phase spaces of  $\Delta R > 0.7$ ,  $P_T^\gamma > 15$  GeV,  $P_T^\gamma > 60$  GeV and  $P_T^\gamma > 90$  GeV, and limits on aTGC coupling constants. The phase space restrictions come from the considerations of the detector acceptance, reducing heavily background-dominated regions and theory.

ATLAS, in addition to the  $P_T^\gamma$  spectrum, total cross section and limits, provides the differential cross section and cross section with different number of associated jets. No evidence of a new physics is observed.

In this dissertation we are measuring total and differential  $d\sigma/dP_T^\gamma$  cross section however we do not derive limits on aTGC coupling constants. The measurement details and results are available in Chapter 5.

659 **3 Experimental Setup**

### 660 3.1 Large Hadron Collider

661 The Large Hadron Collider (LHC) [30], [31], [32] is the largest particle accelerator and the most  
662 ambitious research facility ever built. The LHC is placed into a tunnel originally built for the LEP  
663 accelerator. The LEP was decommissioned to make room for the LHC. The tunnel is about 27 km  
664 in circumference, located at the Swiss-French boundary up to 100 meters undergroud.

665 Before entering LHC, particle beams are going through several stages of the acceleration and  
666 the LHC is the last element of the chain of the CERN's accelerator complex (Fig. 16). Protons  
667 are extracted from hydrogen atoms, are accelerated by Linac2 to energies of 5 MeV, then injected  
668 into the Proton Synchrotron Booster (PSB) where they reach energies of 1.4 GeV. After that  
669 protons are sent to PS and Super PS (SPS) where they are accelerated up to 25 GeV and 450 GeV  
670 respectively. Finally, protons enter the LHC and are accelerated to reach their collision energies  
671 of several TeV per beam. Besides protons, the complex also accelerates and collides lead ions  
672 however in this dissertation we analyze data from proton-proton collisions only and, therefore,  
673 are not discussing lead ion collisions.

675 Main goals of LHC were to detect the SM Higgs boson if it existed and to search for evidences  
676 of BSM physics which may give a clue on understanding the phenomena including but not limited  
677 to the dark matter, the matter-antimatter asymmetry, the nature of the gravitational force. Six  
678 detectors are installed at the LHC to detect particles and perform the relevant measurements.  
679 There are general purpose detectors ATLAS and CMS, there is LHCb which specializes of the  
680 physics of B-mesons, and ALICE which is designed to detect products of heavy ion collisions. In  
681 addition, there are two relatively small detectros: LHCf and TOTEM which are installed close  
682 to the ATLAS and CMS collision points respectively.

684 A new particle with mass  $m = 125$  GeV was discovered by the CMS [3] and the ATLAS [4]  
685 collaborations in 2012. The particle is consistent with the SM Higgs boson predicted by the  
686 EWK sector of the SM. The discovery of the Higgs boson is the greatest achievement by the  
687 LHC to date.

689 While different BSM searches have been constituting a significant part of the LHC physics  
690 program since the beginning of its operation, no deviations from the SM were found by any of  
691 the experiments. The searches continue with higher beam energies and larger amount of data.

694 The design energy of the LHC is 7 TeV per beam however several lower energy points were  
695 and are being probed. In 2010-2011 the LHC operated at energy of 3.5 TeV per beam which was  
696 already higher than energy of any other collider. In 2012 the energy increased up to 4 GeV. In  
697 2013-2014 the LHC was shut down for upgrades. Collisions were restarted at 6.5 TeV in 2015  
698 and the LHC is still operating at this energy in 2016.

700 All important measurements performed at lower energies are also repeated at higher energies  
701 because the ability to probe higher energy scales increases our chances for a discovery and even  
702 if no deviations from the known physics are found at a given energy point, the discovery is still  
703 possible to happen as we go higher in the energy.

704 In addition to the beam energy, there are many other collider parameters. A brief summary  
705 of them is available in Tab. 2. One of the most important parameters of an accelerator is the  
706 ability to produce a large number of interesting collisions which is determined by the luminosity.  
707 The instantaneous luminosity is determined by the following expression [5]:

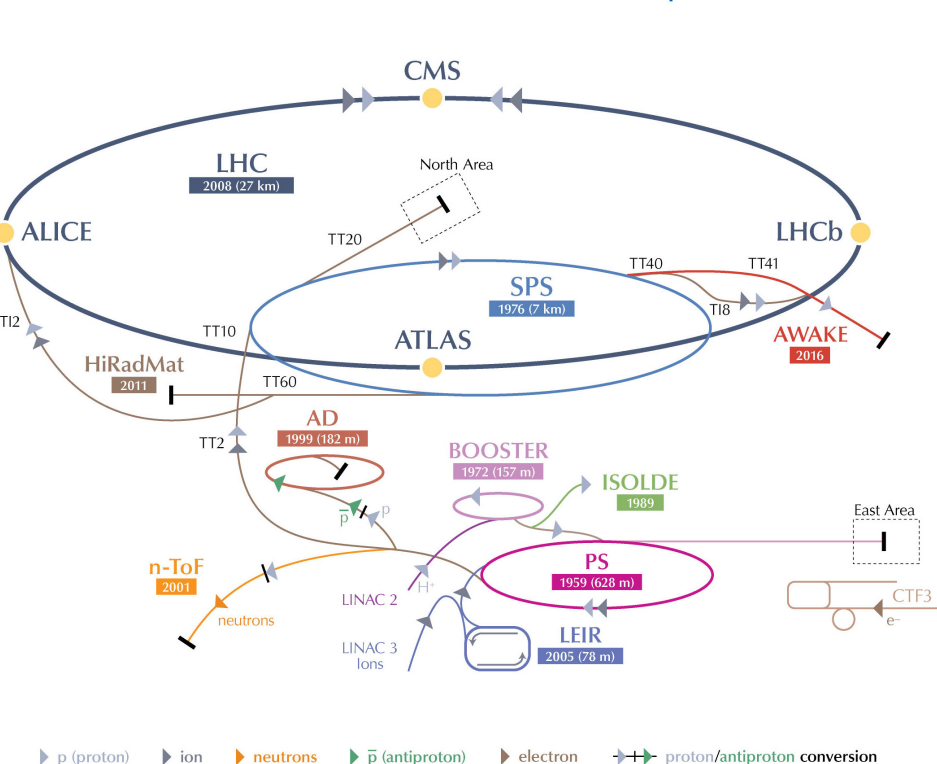
710 
$$L = f \frac{n_1 n_2}{4\pi\sigma_x\sigma_y}$$

711 where  $n_1$  and  $n_2$  are numbers of particles in colliding bunches,  $f$  is a frequency of collisions,  
712  $\sigma_x$  and  $\sigma_y$  are beam sizes in horizontal and vertical directions. To determine the integrated  
713 luminosity, one has to integrate the instantaneous luminosity over time:

$$L_{int} = \int L dt$$

The luminosity of the LHC is also higher than of any previously existed collider. The integrated luminosity of the LHC for different years of the operation are shown in Fig. 17. Run periods of LHC in 2010-2012 refer to Run I of the LHC operation. While working on energy of  $\sqrt{s} = 7$  TeV, LHC delivered  $44.96 \text{ pb}^{-1}$  and  $6.1 \text{ fb}^{-1}$  of data in 2010 and 2011 year respectively. In 2012 the working energy of LHC was  $\sqrt{s} = 8$  TeV, and the integrated luminosity was  $L_{int} = 23.3 \text{ fb}^{-1}$ . After a long shutdown, LHC was upgraded for Run II, to operate on  $\sqrt{s} = 13$  TeV in 2015 and delivered  $4.22 \text{ fb}^{-1}$  of data by the end of 2015. In 2016 LHC continues operation on  $\sqrt{s} = 13$  TeV and by the end of September the integrated luminosity already exceeded a value of  $30 \text{ fb}^{-1}$  [36].

The measurement of this dissertation is performed at the energy of 4 TeV per beam or at the center of mass energy  $\sqrt{s} = 8$  TeV with  $19.6 \text{ fb}^{-1}$  of data. The same process was measured at  $\sqrt{s} = 7$  TeV with about four times less amount of data by both CMS and ATLAS. These measurements are discussed in greater details in Ch. 2.5.



LHC Large Hadron Collider SPS Super Proton Synchrotron PS Proton Synchrotron

AD Antiproton Decelerator CTF3 Clic Test Facility AWAKE Advanced WAKEfield Experiment ISOLDE Isotope Separator OnLine Dvice

LEIR Low Energy Ion Ring LINAC LINear ACcelerator n-ToF Neutrons Time Of Flight HiRadMat High-Radiation to Materials

© CERN2013

Figure 16: CERN's accelerator complex. Source of the figure: [33].

Table 2: Main parameters of LHC [30]

|                                     |  |
|-------------------------------------|--|
| Circumference                       | 27 km                                    |
| Dipole operating temperature        | 1.9 K                                    |
| Number of magnets                   | 9593                                     |
| Number of main dipoles              | 1232                                     |
| Number of main quadrupoles          | 392                                      |
| Number of RF cavities               | 8 per beam                               |
| Nominal energy, protons             | 7 TeV                                    |
| Nominal energy, lead ions           | 2.76 TeV per nucleon                     |
| Peak magnetic dipole field          | 8.33 T                                   |
| Min. distance between bunches       | 7 m                                      |
| Design luminosity                   | $10^{34} \text{ cm}^{-2} \text{ s}^{-1}$ |
| No. of bunches per proton beam      | 2808                                     |
| No. of protons per bunch (at start) | $1.1 \times 10^{11}$                     |
| No. of collisions per second        | 600 millions                             |

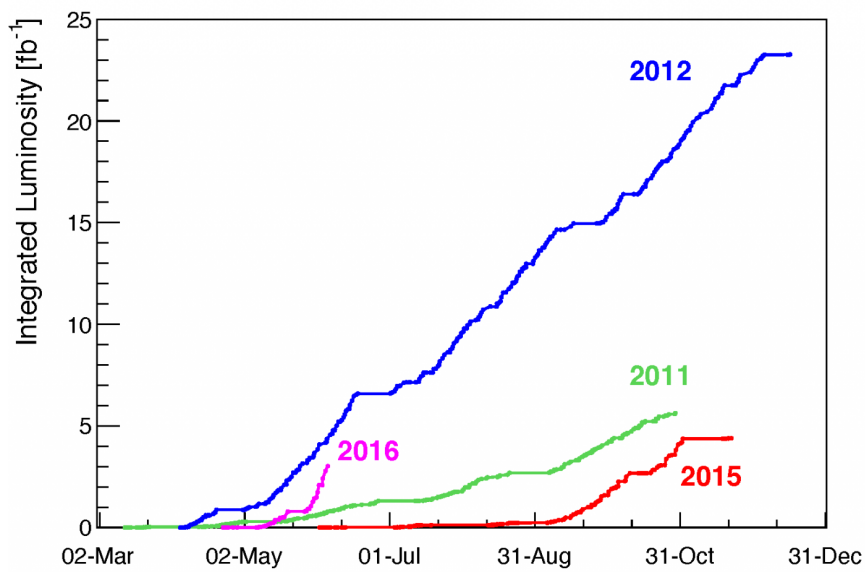


Figure 17: LHC integrated luminosity by year. Source of the figure: [34].

### 3.2 Compact Muon Solenoid

#### 3.2.1 Introduction

The CMS is a general-purpose detector designed for detecting various highly energetic particles which are being produced in pp collisions at the LHC. The CMS has a broad program with goals of direct and indirect searches of the BSM physics including but not limited to supersymmetric particles. Its main feature is a huge magnet to create a magnetic field of 4T to curve charged particles in the tracking system and 2T outside to curve muons in the muon system.

The CMS detector is a cylindrically symmetric with a colliding beam as a central axis. Cartesian, cylindrical and spherical coordinates are all used to describe the CMS geometry, depending on the context. The  $x$ -axis of the CMS points towards the center of the LHC while the  $y$ -axis points vertically up. The direction of the  $z$ -axis corresponds to the counterclockwise direction of the LHC beam (Fig. 18, left). Cylindrical coordinates are defined as  $r = \sqrt{x^2 + y^2}$ ,  $\phi = \arctan(y/x)$ . Instead of the polar angle  $\theta$ , it is more convenient to use the pseudorapidity  $\eta = -\ln \tan \theta/2$ . A pseudorapidity changes from  $\eta = -\infty$  to  $\eta = +\infty$  for directions parallel to the beam axis with the value of  $\eta = 0$  for a direction perpendicular to the beamlime. This variable is convenient for measurements because a distribution of a massless particle in  $\eta$  is nearly flat. The acceptance of the CMS in  $\eta$  is limited and varies from  $|\eta| = 2.4$  to  $|\eta| = 5.0$  depending on a subdetector.

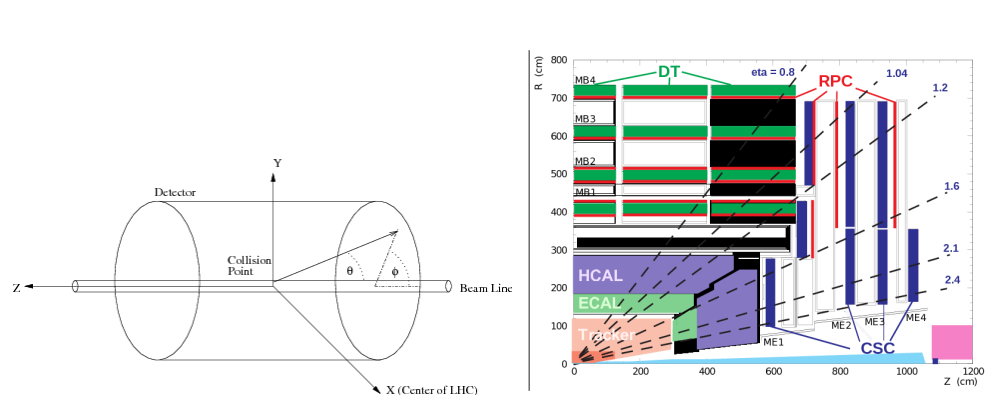


Figure 18: Left: CMS coordinate system. Right: pseudorapidity ranges for different CMS subdetectors.

The detector consists, from inner to outer layer, of a tracking system, an electromagnetic calorimeter (ECal), a hadronic calorimeter (HCal), a magnet and a muon system. Having the tracking system, ECal and HCal inside of a large solenoid makes the detector compact. A segment of a CMS slice in  $r - \phi$  plane is shown in Fig. 19.

When a heavy particle is produced in a collision, it decays immediately, and we detect its long-living decay products including an electron, a photon, a muon, a neutral hadron or a charged hadron. Depending on the trace left by a particle in different subdetectors we can identify a particle. Electrons and positrons leave curved tracks in the tracking system and then induce showers in the electromagnetic calorimeter (ECal). Photons induce the same electromagnetic showers in ECal however, as neutral particles, they do not leave tracks in the tracking system. Hadrons normally travel through the ECal undisturbed and induce a hadronic shower in the hadronic calorimeter (HCal). Charged and neutral hadrons can be distinguished from each other by checking whether they leave a track in the tracking system or not. Muons are the only particles which penetrate through the ECal, the HCal and the magnet and leave tracks in the CMS muon system. Neutrinos are not detected by CMS.

768

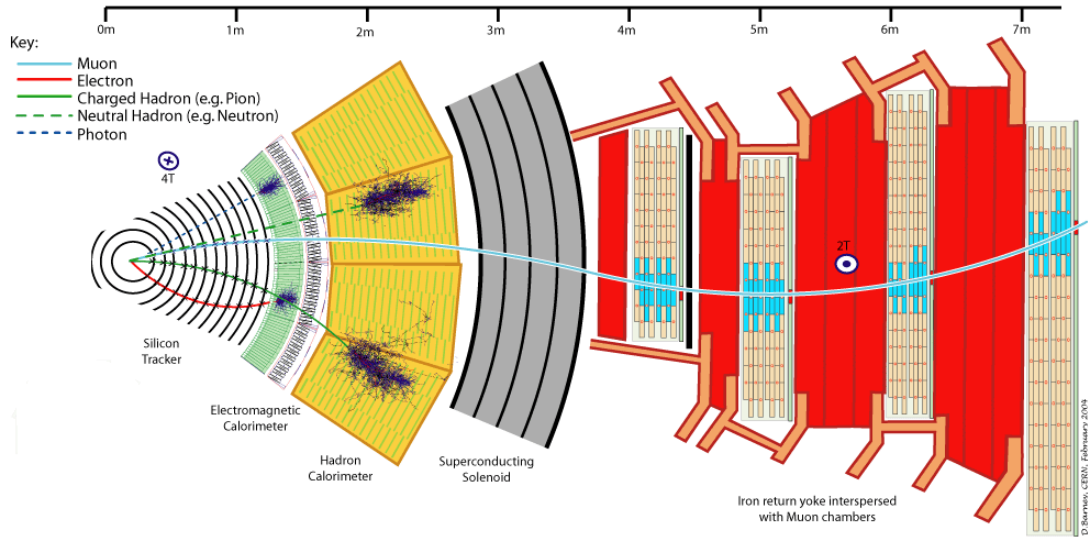


Figure 19: CMS slice.

769 All subdetectors are important for the  $W\gamma$  measurement and the remainder of this chapter  
 770 describes the subdetectors in greater details. Muons and electrons which we have as final state  
 771 particles are both affected by CMS magnetic field allowing the tracking system and the muon  
 772 system to measure their trajectory parameters and momenta. In this dissertation we use the  
 773 information of the primary vertex determined by the tracking system to select our events. Also  
 774 the tracker provide us the information about electrons trajectories and momenta in the electron  
 775 channel and distinguishes between electrons and photons.  
 776

### 777 3.2.2 Magnet

778 A magnetic field in a particle detector is necessary to measure momenta of charged particles  
 779 by track curvatures. The higher the momentum is, the less a particles's path is affected by the  
 780 magnetic field. In CMS it is done in the tracking system for all charged particles and in the  
 781 muon system for muons.  
 782

783 The CMS magnet is placed between layers of HCal and a muon system. It creates a magnetic  
 784 field of 4T inside the magnet, for the tracking system, and 2T outside the magnet, for the muon  
 785 system. It is necessary to have stronger field in the tracking system because a density of tracks  
 786 is much higher there than in the muon system and also the tracking system is much smaller and,  
 787 therefore, more significant curvature is necessary to measure the momentum with high precision.  
 788

789 The magnet is made of superconducting wires. An electric current flowing in the wires creates  
 790 a uniform field inside the solenoid and also provides a magnetic field of a certain configuration  
 791 outside the solenoid.  
 792

### 793 3.2.3 Tracking System

794 The tracking system measures track geometry including particles trajectories and locations of  
 795 primary and secondary vertices and momenta of charged particles. It needs to disturb particles

as little as possible so that they can pass through. Therefore, just a few measurements must be enough to reconstruct the track. The accuracy of a measurement of each hit is  $10 \mu\text{m}$ .

The tracking system consists of silicon pixels and silicon strips (Fig. 20). Collision tracks start at the center and then cross the layers of the tracking system. Tracks are straight in  $r - z$  plane and curved by the magnetic field in the  $r - \phi$  plane. The acceptance of the tracker system in  $r - z$  plane is geometrically limited by  $\eta = 2.5$  ( $\eta = -\ln[\tan \theta/2]$ , where  $\theta$  is a polar angle).

The pixel tracker is the closest subsystem of CMS to the collision point thus it experiences the largest particle flux: at 8 cm from the collision point the flux is about 10 million  $1/(\text{cm}^2\text{s})$ , and the pixel detector with its 65 millions sensors is capable to reconstruct all these tracks. It consists of three layers of cylinders in the barrel with radii of 4 cm, 7 cm and 11 cm and four disks in the endcap, two disks at each side. The tracker is designed in such a way that a single track hits multiple sensors. Then the trajectory is reconstructed based on how much charge is collected on each sensor. This allows us to reach a spacial resolution of 15-20  $\mu\text{m}$  which is much smaller than a distance between sensors.

The strip tracker is placed right after the pixel tracker and occupies the detector volume up to 130 cm around the beam axis. The strip tracker consists of four parts: the tracker inner barrel (TIB), the tracker inner disks (TID), the tracker outer barrel (TOB) and the tracker endcap (TEC) as shown in Fig. 20. In the strip tracker there are over 15,000 sensitive modules with a total number of 10 million strips. Each sensitive module consists of a set of sensors, its support structure and readout elements.

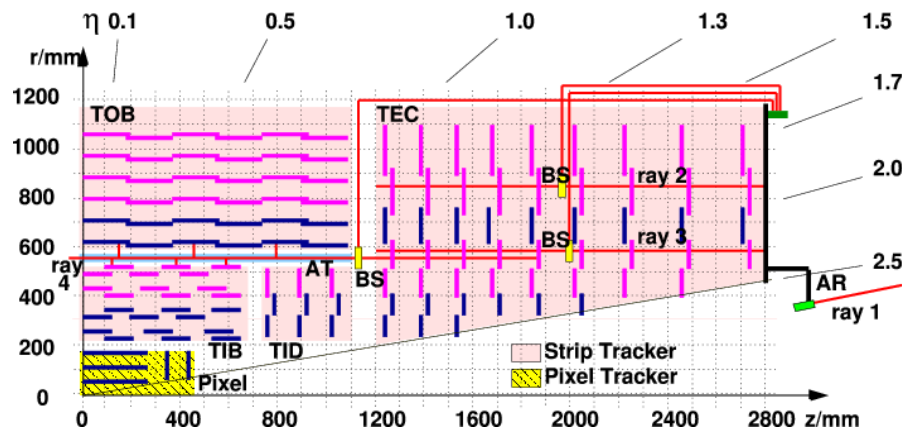


Figure 20: Slice of the CMS tracking system in  $r - z$  plane.

### 3.2.4 Electromagnetic Calorimeter

The ECal measures energy of electrons and photons and also measures geometries of their trajectories. Electrons and photons interact with the ECal substance by inducing electromagnetic showers. Traces left by photons and electrons in the ECal are the same. To distinguish between these two particles, it is necessary to perform matching to the track in the tracking system. If there is a track, then there is an electron (or positron). If there is no track, then the particle is a photon.

The Ecal is a layer between the tracking system and the HCal. It is made of high-density lead tungstate crystals arranged in a barrel section and two endcap sections. The crystals work as scintillators. When electrons and photons pass through it, it produces light proportional to the

831 particle's energy. The scintillated light then is amplified by photomultipliers producing signals  
832 on sensitive elements.

833 It is important for the ECal to be able to distinguish between high energetic photons and  
834 pairs of lower energetic photons e.g. from a  $\pi^0$  decay. It is especially difficult in the endcap  
835 sections where angle between two photon trajectories is small. Ecal preshower located in front  
836 of the endcaps which have much smaller granularity provide extra spacial precision. Their strips  
837 are 2 mm wide compared to 3 cm wide crystals in the main volume of the ECal.  
838

839

#### 840 **3.2.5 Hadron Calorimeter**

841 The HCal is placed right after the ECal and is the last subdetector within the magnet. The  
842 HCal measures energies of charged and neutral hadrons. In addition, the HCal determines the  
843 track parameters. Match to the tracking system has to be done: if a matching track found, then  
844 it is a charged hadron otherwise it is a neutral hadron.

845

846 The HCal consists of alternate layers of absorbers and scintillators. Hadrons hit brass or steel  
847 plate of absorber producing secondary particles. When emerge into the scintillator, the particles  
848 induce hadronic and electromagnetic showers and emit blue-violet light which is further shifted  
849 to the green region and read out by special boxes within the HCal. The secondary hadrons pro-  
850 duced during the interaction with the absorber interact with the next absorber producing more  
851 showers in the next layers of scintillators and also affect the total energy deposit. All hadrons  
852 must be stopped inside the layers of the HCal.

853

#### 854 **3.2.6 Muon System**

855 Muons pass through the ECal, the HCal and the magnet without interacting. They are the only  
856 particles which are registered in the muon system which is placed outside the magnet and which  
857 is the largest part of CMS detector.

858

859 There are four concentric layers of muon detectors (stations) and iron return yoke between  
860 them. Muons induce several hits in the muon stations which are later fitted and matched to the  
861 tracking system measurements to provide the best possible resolution in the measurements of all  
862 parameters of the muon's trajectory and momentum.

863

864 There are three types of muon chambers used in the CMS muon system: drift tubes (DTs),  
865 cathode strip chambers (CSCs) and resistive plate chambers (RPCs). Overall, there are 1400  
866 muon chambers including 250 DTs, 540 CSCs and 610 RPCs.

867

868 The system of DTs measures positions of muons in the barrel. Each DT chamber is about 2 m  
869 by 2.5 m in size. It consists of 12 layers of aluminium which are grouped by four. There are up  
870 to 60 drift tubes in a layer. The middle group of layers measures  $z$ -coordinate and two other  
871 groups determine the perpendicular coordinate.

872

873 Each drift tube is 4 cm in width, is filled with a gas and has a wire inside. When a charged  
874 particle passes through the volume, it ionizes atoms and the wire receives an electric charge.

875

876 CSCs are placed in endcap regions. CSCs are arrays of anode wires which are crossed by  
877 copper cathode strips placed in a gas volume. When a charged particle penetrates to the gas  
878 volume, it ionizes the gas. Electrons drift to the wires while ions move to the strips. Strips are  
879 perpendicular to wires, thus, we measure two coordinates for each particle.

880

881 RPCs are parallel capacitors made of high-resistivity plastic plates with a space between  
882 them filled with a gas. RPCs provide quick measurements of muon momenta and are used for

883 triggering.

884

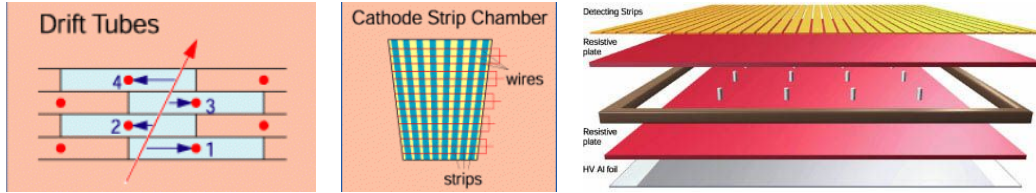


Figure 21: Components of the CMS muon system. Left to right: drift tubes, cathode strip chambers (CSCs), resistive plate chambers (RPCs).

### 885 3.2.7 Triggering and Data Aquisition

886 At peak luminosity, CMS experiences one billion proton-proton collisions per second which come  
887 in bunches separated just by 25 ns from one other. New events come before the events from  
888 the previous bunch crossing left the detector. To process the information from many different  
889 collisions at the same time, data is stored in pipelines.

890

891 It is not technically possible to readout all these events. Moreover, we do not need most  
892 of these events for a physics analysis because most of these events do not have a potential to  
893 discover a new physics. We have resources to store about one hundred events out of one billion  
894 that is why we need a trigger system which quickly decides what the best one hundred events are.

895

896 If the triggers were too loose, and we would select one hundred events too quickly, e.g., out  
897 of a hundred million events, then CMS would not be able to process the rest 90% of events in a  
898 givem set of one billion and we would lose 90% of potentially interesting events.

899

900 If the triggers were too strict, we would select, e.g, ten events out of one billion, not one  
901 hundred and lose CMS potential to store and process data by 90% which would significantly  
902 reduce our chances for a discovery.

903

904 Thus, the challenge of the trigger system is to select the best one hundred events out of one  
905 billion and do that fast to be able to process every single event. To achive this goal, a two-level  
906 trigger system was developed consisting from the Level 1 (L1) trigger and the high level trigger  
907 (HLT) as shown in Fig. 22.

908

909 L1 is a hardware based trigger (Fig. 23). It uses information from the ECal, HCal and muon  
910 system. L1 reduces frequency of coming events from 40 MHz to 100 kHz. Events which did not  
911 pass the L1 trigger are lost forever while events which pass the L1 trigger are temporarily stored  
912 to get checked by the HLT.

913

914 HLT is a software-based trigger. It uses information from all subdetectors and runs quick  
915 reconstruction and identification algorithms to determine types of particles and their kinematics.  
916 It reduces the number of events to 100 Hz. Events which did not pass HLT are lost forever.  
917 Events which pass HLT are arranged into appropriate datasets depending on HLT selection cri-  
918 teria they passed and stored for physics analyses.

919

### 920 3.2.8 Event Reconstruction

921 Where to place particle reconstruction, particle flow algorithm and MET? Check other theses

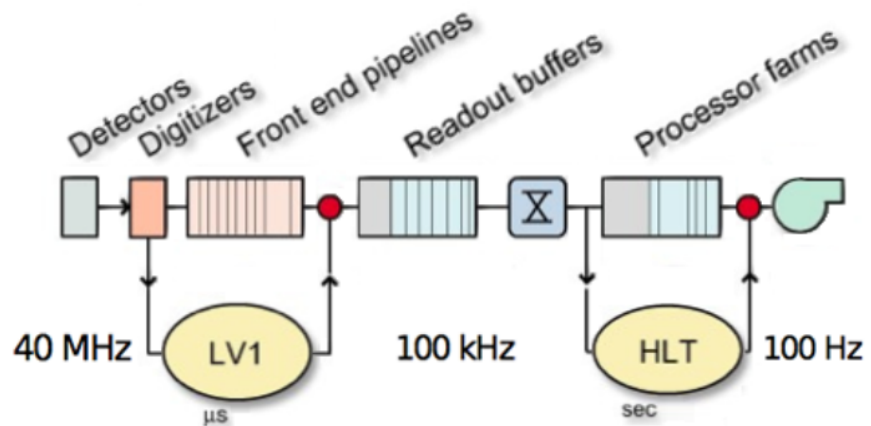


Figure 22: Two-level CMS trigger system.

922       Acceptance: particles which are too collinear and go to pipe; particles which get curved too  
923       strongly

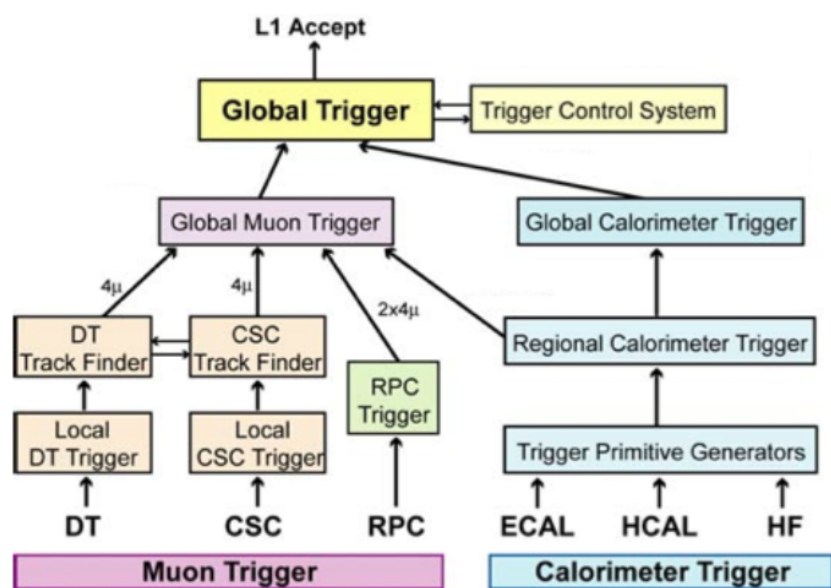


Figure 23: Level 1 CMS trigger system.

924 **4 CMS Tracker Alignment**

## 925 4.1 Algorithm

926 Why align?

927 How to align?

928 When align?

929 How to check that your alignment is good?

930 A tracking system detects hits produced by a charged particle traveling through the detector.  
 931 In a presence of a constant magnetic field the particle has a helical trajectory. A reconstruction  
 932 algorithm determines the track parameters by fitting the positions of hits assuming the helix  
 933 trajectory.

934 Better hit resolution and the location uncertainty lead to better precision of a measurement  
 935 of the track parameters. The location uncertainty depends on our knowledge of the positions and  
 936 orientations in space of the tracking system modules. The hit resolution in the CMS pixel detector  
 937 is  $\sim 15 \mu\text{m}$ . When the modules are mounted, their positions are known with precision of  $\sim 200 \mu\text{m}$ .  
 938 Thus, we need to know positions of modules 20 times better than they are known when mounted.

939 The procedure of the determination of the modules locations and orientations is called the  
 940 tracker alignment. The concept of the track-based alignment can be illustrated in the example of  
 941 the alignment of a toy tracker. When a charged particle passing through a detector (Fig. 24, top  
 942 left) it crosses a toy tracker which consists of six flat equidistant modules (Fig. 24, top right). If  
 943 the modules were placed exactly at their designed positions, we would observe the hits exactly at  
 944 the points where the track crosses modules at the points of ideal geometry (Fig. 24, middle left).  
 945 However, in a reality the positions and tilts of the modules are different from ones suggested by  
 946 the ideal geometry (Fig. 24, middle right). Hits, indeed, are recorded at the places where mod-  
 947 ules are actually mounted, not at the design ideal places (Fig. 24, bottom left). If we assumed a  
 948 tracker to be ideal and a track to be smooth, we would see that our hits are off-track (Fig. 24,  
 949 bottom right). So, we recalculate positions of the modules so that all the hits are laying on the  
 950 same smooth track (Fig. 25, top left). But these recalculated positions still do not coincide with  
 951 the actual positions (Fig. 25, top right). Then we record more and more tracks (Fig. 25, middle  
 952 left and right). We take into account them all and determine the alignment parameters with  
 953 necessary precision (Fig. 25, bottom left and right).

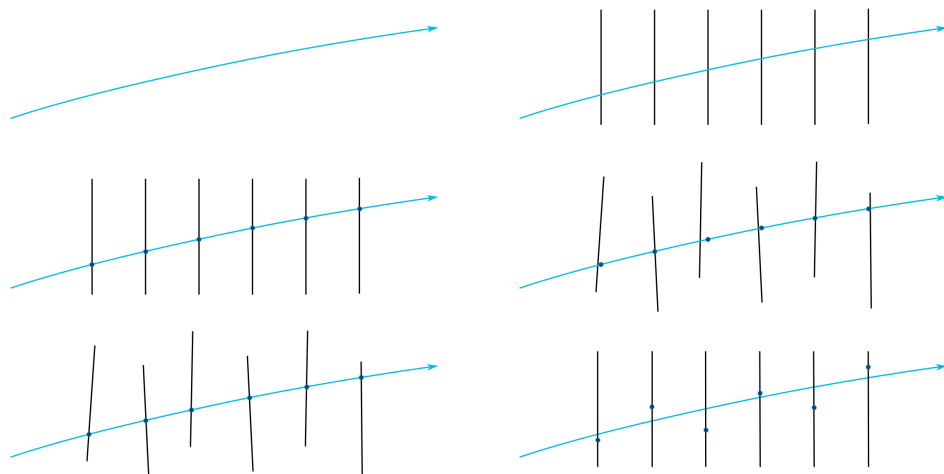


Figure 24: The alignment of a toy tracker, part 1.

958 When we record a track with a not-aligned tracker, we see that the track is not smooth. But

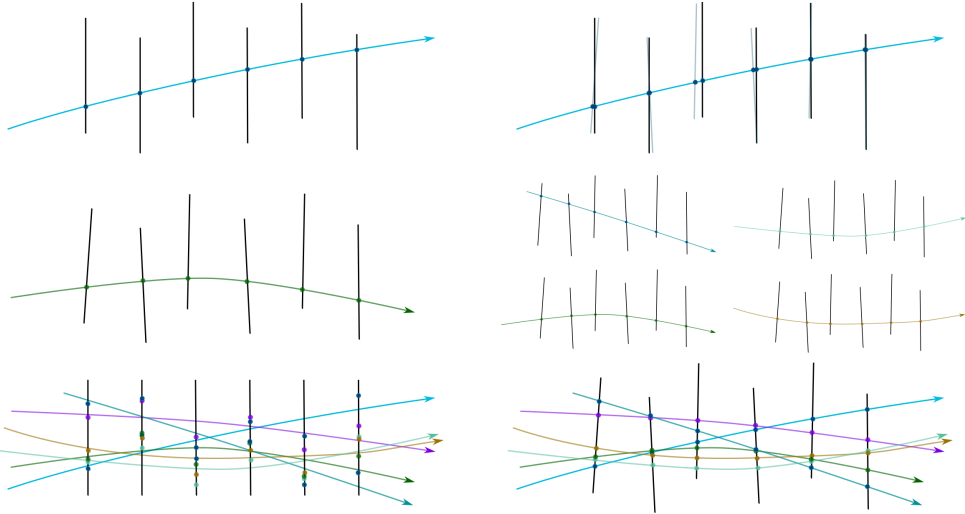


Figure 25: The alignment of a toy tracker, part 2.

that is because our knowledge of module positions is not exact. Thus, we can correct the positions assuming the track is smooth. But when we process the next track, we may find out that the positions have to be corrected again. Thus, we record many tracks and minimize residuals between measured and predicted hits.

The CMS tracker contains 1440 silicon pixel modules in PXB and PXF and 15148 silicon strip modules in TIB, TOB, TID, TEC.

The tracker alignment problem is the least squared problem. The expression to minimize is the following:

$$\chi^2(\mathbf{p}, \mathbf{q}) = \sum_j^{\text{tracks}} \sum_i^{\text{tracks}} \left( \frac{m_{ij} - f_{ij}(\mathbf{p}, \mathbf{q}_j)}{\sigma_{ij}} \right)^2 \quad (36)$$

where  $\mathbf{p}$  are parameters describing the tracker geometry,  $\mathbf{q}_j$  are parameters of the  $j^{th}$  track,  $m_{ij} - f_{ij}$  are residuals, distances between the measured hit and a position predicted by the track fit,  $\sigma_{ij}$  is the Gaussian error of the measurement.

We can align the large substructures and individual modules with respect to their substructures. The parameters to align large substructures include their positions and orientations of the subdetectors (rotations). Thus, each subsystem is described by six parameters: three coordinates X, Y, Z and three angles  $\alpha$ ,  $\beta$ ,  $\gamma$ . At the module level, we align positions and rotations with respect to the position s and angles of the corresponding large structure (Fig. 26). In addition, at the module level we align for surface deformations which are described by three parameters per sensor (Fig. 27).

A track can be described with five parameters.

We have two alignment algorithms: Millepede and HIP. Millepede performs a simultaneous fit of all alignment parameters and all track parameters while HIP perform iterative fits of alignment parameters  $\mathbf{p}$  and track parameters  $\mathbf{q}_j$ .

It is important to use different sorts of tracks for the alignment. Cosmic tracks pass through the detector vertically and do not allow us to connect different subdetectors to one another.

989 Collision tracks originate from the collision point and go in all directions. However, those tracks  
 990 which cross TEC are all almost collinear and, therefore, it is difficult to measure  $z$ -coordinate of  
 991 TEC modules with collision tracks only.

992

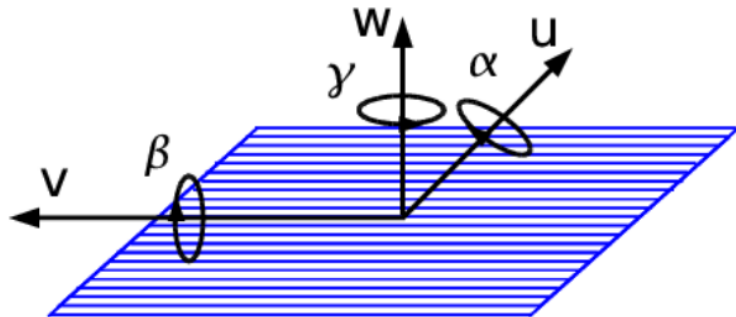


Figure 26: Alignment parameters.

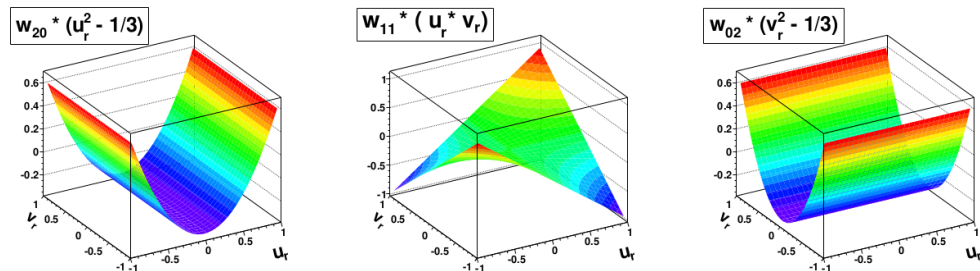


Figure 27: Surface deformations.

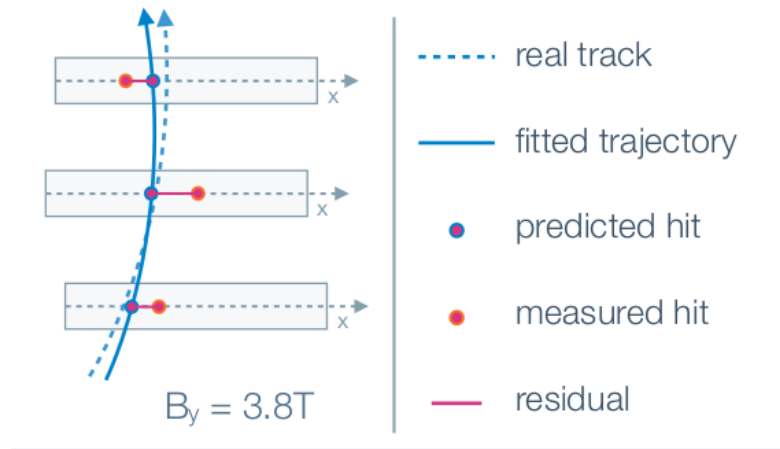


Figure 28: Track residuals.

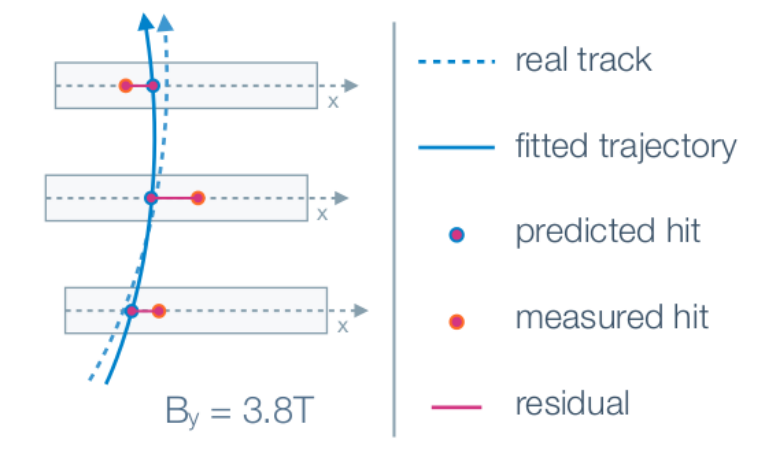


Figure 29: Track residuals.

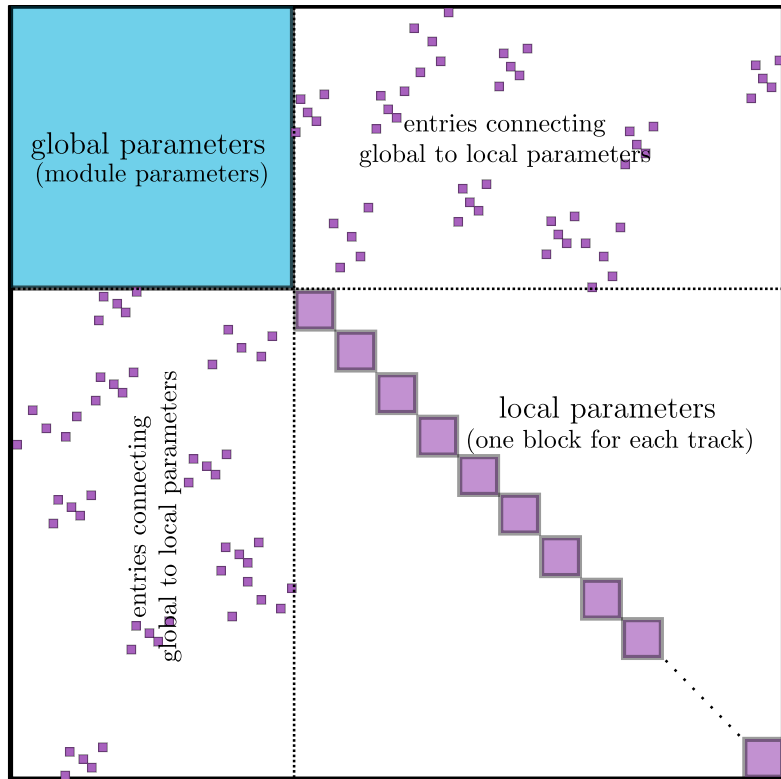


Figure 30: Track residuals.

993 **4.2 Selected Results**

994 CRUZET, CRAFT and first collisions of 2015

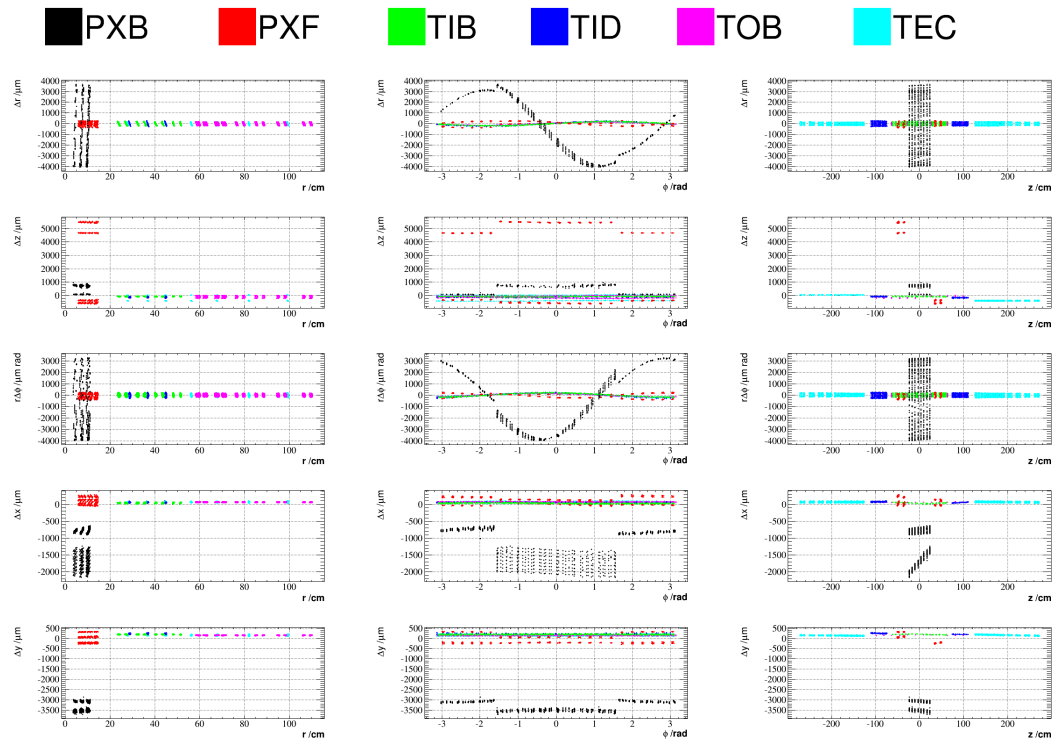


Figure 31: Geometry comparison plot of CRUZET 2015 object vs Run I.

**995 5 W $\gamma$  Cross Section Measurement**

996 Place analysis outline here

## 997 References

- 998 [1] Griffiths textbook  
999 [2] website: <http://www.isgtw.org/spotlight/go-particle-quest-first-cern-hackfest>  
1000 [3] CMS Paper about Higgs boson discovery  
1001 [4] ATLAS Paper about Higgs boson discovery  
1002 [5] PDG  
1003 [6] website: <https://science.nasa.gov/astrophysics/focus-areas/what-is-dark-energy>  
1004 [7] Pich lectures: The Standard Model of Electroweak interactions  
1005 [8] Halzen, Martin "Quarks and leptons"  
1006 [9] <http://iopscience.iop.org/article/10.1088/0034-4885/70/1/R02>  
1007 [10] Peskin, Schroeder  
1008 [11] Lindsey's thesis (CMS Zg- $\zeta$ llg, 7 TeV)  
1009 [12] website: [https://www-d0.fnal.gov/results/publications\\_talks/thesis/snyder/html/node17.html](https://www-d0.fnal.gov/results/publications_talks/thesis/snyder/html/node17.html)  
1010 [13] website: [https://en.wikipedia.org/wiki/Cross\\_section\\_%28physics%29](https://en.wikipedia.org/wiki/Cross_section_%28physics%29)  
1011 [14] LO (1969) theory paper  
1012 [15] NNLO theory paper  
1013 [16] NLO theory paper  
1014 [17] aTGC paper  
1015 [18] Senka's thesis (CMS Wg- $\zeta$ munug, 7 TeV)  
1016 [19] D0 Combination of  $W\gamma$ , WW, WZ and VW using 8.6 fb-1 of 2 TeV  $p\bar{p}$  collisions Phys.Lett.  
1017 B718 (2012) 451-459  
1018 [20] LEP Combination of WW and single W using 0.7 fb-1 per experiment of  $e^+e^-$  collisions at  
1019 WW pair production energies arXiv:1302.3415  
1020 [21] 7TeV Wg ATLAS paper  
1021 [22] ATLAS WW using 20.3 fb-1 of 8 TeV pp collisions Submitted to JHEP  
1022 [23] ATLAS VW ( $V=W,Z \rightarrow jj$ ) using 4.6 fb-1 of 7 TeV pp collisions JHEP 01 (2015) 049  
1023 [24] website: [https://twiki.cern.ch/twiki/bin/view/CMSPublic/PhysicsResultsSMPaTGC#Figure\\_1\\_Limits\\_on\\_WW](https://twiki.cern.ch/twiki/bin/view/CMSPublic/PhysicsResultsSMPaTGC#Figure_1_Limits_on_WW)  
1024 [25] 7TeV Wg CMS paper  
1025 [26] CMS WW using 4.9 fb-1 of 7 TeV pp collisions Eur. Phys. J. C 73 (2013) 2610  
1026 [27] CMS WW using 19.4 fb-1 of 8 TeV pp collisions Submitted to EPJC  
1027 [28] CMS VW ( $V=W,Z \rightarrow jj$ ) using 5.0 fb-1 of 7 TeV pp collisions Eur.Phys.J. C73 (2013) 2283  
1028 [29] CMS 8 TeV WW lnlnmu  
1029 [30] CMS 7 TeV Zg nunug  
1030 [31] CERN brochure, <http://cds.cern.ch/record/1165534/files/CERN-Brochure-2009-003-Eng.pdf>

- 1032 [32] LHC TDR
- 1033 [33] website: <http://home.cern/topics/large-hadron-collider>
- 1034 [34] website: <http://cds.cern.ch/record/1621583/files/>
- 1035 [35] [http://home.cern/sites/home.web.cern.ch/files/image/update-for\\_cern\\_people/2016/06/intlumirunall\\_image.png](http://home.cern/sites/home.web.cern.ch/files/image/update-for_cern_people/2016/06/intlumirunall_image.png)
- 1036 [36] website: <http://cds.cern.ch/journal/CERNBulletin/2014/24/News%20Articles/1706606>
- 1037 [37] website: <https://twiki.cern.ch/twiki/bin/view/CMSPublic/LumiPublicResults>
- 1038